The Astrophysical Journal, 1007:184 (22pp), 2026 August 20 https://doi.org/10.3847/1538-4357/ae8a46

SN 2022erq: A Superluminous Thermonuclear Supernova with Escalating Preexplosion Mass Loss

Qian Zhai[1], Jujia Zhang[1], Xiaofeng Wang[2], A. Pastorello[3], Alexei V. Filippenko[4], József Vinkó[5,6,7], Thomas G. Brink[4], Yunkun Han[1], G. Valerin[3], N. Elias Rosa[3,8], Yongzhi Cai[1,3], Weili Lin[9], Yi Yang[2], WeiKang Zheng[4], Xiangcun Meng[1], Chengyuan Wu[1], Liping Li[1], Zeyi Zhao[1], J. Craig Wheeler[7], Jose L. Prieto[10], Jialian Liu[2], Gaici Li[2], Shengyu Yan[2], Fangzhou Guo[2], C. P. Gutiérrez[8,11], E. Kankare[12], Peter Lundqvist[13], S. Moran[14], A. Reguitti[3,15], I. Salmaso[3,16], M. D. Stritzinger[17], S. Williams[12,18], J.-W. Zhao[19], D.-D Shi[20], Jianrong Shi[21], Z.-H. Peng[22], Tengfei Song[1], Yongyuan Xiang[1], Attila Bódi[5,23], Borbála Cseh[5,24], Ágoston Horti-Dávid[5,25], Csilla Kalup[5,25], Levente Kriskovics[5], Réka Könyves-Tóth[5,6], András Pál[5], Bálint Seli[5,25], Ádám Sódor[5], Róbert Szakáts[5], P. A. Mazzali[26,27], T. Kravtsov[28,18], K. Matilainen[28], T. M. Reynolds[12,29,30], L. Galbany[8,11], and Bo Wang[1]

[1] International Centre of Supernovae (ICESUN), Yunnan Key Laboratory of Supernova Research, Yunnan Observatories, Chinese Academy of Sciences (CAS), Kunming 650216, People's Republic of China; jujia@ynao.ac.cn
[2] Physics Department, Tsinghua University, Beijing 100084, People's Republic of China
[3] INAF—Osservatorio Astronomico di Padova, Vicolo dell'Osservatorio 5, 35122 Padova, Italy
[4] Department of Astronomy, University of California, Berkeley, CA 94720-3411, USA
[5] HUN-REN CSFK Konkoly Observatory, MTA Centre of Excellence, Konkoly Thege M. út 15-17, Budapest, 1121, Hungary
[6] Department of Experimental Physics, Institute of Physics, University of Szeged, Dóm tér 9, Szeged, 6720, Hungary
[7] Department of Astronomy, University of Texas at Austin, 2515 Speedway, Stop C1400, Austin, TX 78712-1205, USA
[8] Institute of Space Sciences (ICE, CSIC), Campus UAB, Carrer de Can Magrans, s/n, E-08193 Barcelona, Spain
[9] Department of Astronomy, Xiamen University, Xiamen, Fujian 361005, People's Republic of China
[10] Instituto de Estudios Astrofísicos, Facultad de Ingeniería y Ciencias, Universidad Diego Portales, Avenida Ejército Libertador 441, Santiago, Chile
[11] Institut d'Estudis Espacials de Catalunya (IEEC), 08860, Castelldefels (Barcelona), Spain
[12] Tuorla Observatory, Department of Physics and Astronomy, University of Turku, FI-20014 Turku, Finland
[13] The Oskar Klein Centre, Department of Astronomy, Stockholm University, AlbaNova, SE-10691, Stockholm, Sweden
[14] School of Physics and Astronomy, University of Leicester, University Road, Leicester LE1 7RH, UK
[15] INAF—Osservatorio Astronomico di Brera, Via E. Bianchi 46, 23807, Merate (LC), Italy
[16] INAF—Osservatorio Astronomico di Capodimonte, Salita Moiariello 16, 80131 Napoli, Italy
[17] Department of Physics and Astronomy, Aarhus University, Ny Munkegade 120, DK-8000 Aarhus C, Denmark
[18] Finnish Centre for Astronomy with ESO (FINCA), Quantum, Vesilinnantie 5, University of Turku, FI-20014 Turku, Finland
[19] South-Western Institute for Astronomy Research, Yunnan Key Laboratory of Survey Science, Yunnan University, Kunming, Yunnan 650500, People's Republic of China
[20] Center for Fundamental Physics, School of Mechanics and opticelectrical Physics, Anhui University of Science and Technology, Huainan, Anhui 232001, People's Republic of China
[21] National Astronomical Observatories, Chinese Academy of Sciences, Beijing 100101, People's Republic of China
[22] School of Electronic Science and Engineering, Chongqing University of Posts and Telecommunications, Chongqing 400065, People's Republic of China
[23] Department of Astrophysical Sciences, Princeton University, Peyton Hall, 4 Ivy Lane, Princeton University, Princeton, NJ 08544, USA
[24] MTA-ELTE Lendület "Momentum" Milky Way Research Group, Hungary
[25] ELTE Eötvös Loránd University, Institute of Physics and Astronomy, Pázmány Péter sétány 1A, Budapest 1117, Hungary
[26] Astrophysics Research Institute, Liverpool John Moores University, Liverpool Science Park, 146 Brownlow Hill, Liverpool L3 5RF, UK
[27] Max-Planck-Institut für Astrophysik, Karl-Schwarzschild Str. 1, D-85741 Garching, Germany
[28] Department of Physics and Astronomy, University of Turku, FI-20014 Turku, Finland
[29] Niels Bohr Institute, University of Copenhagen, Jagtvej 128, 2200 Copenhagen N, Denmark
[30] Cosmic Dawn Center (DAWN)
Received 2025 December 22; revised 2026 June 28; accepted 2026 July 7; published 2026 August 18

Abstract

We present a photometric and spectroscopic study of the superluminous Type Ia supernova SN 2022erq. Its early spectra, dominated by iron-group elements with weak intermediate-mass features, might indicate highly efficient nuclear burning, broadly similar to that inferred for some overluminous Type Ia supernovae. The rapid emergence and persistence of narrow Balmer emission lines superposed on this iron-rich spectrum provide clear evidence of long-lived interaction with a hydrogen-rich circumstellar medium (CSM), establishing SN 2022erq as a member of the rare Ia–CSM class. SN 2022erq reached a peak bolometric luminosity of $\sim 8 \times 10^{43}$ erg s^{-1} and exhibited an exceptionally slow postpeak decline, indicating that its light curve is dominated by long duration ejecta–CSM interaction. By combining Hα diagnostics with bolometric light-curve modeling, we reconstruct the preexplosion mass-loss history of the progenitor. The mass-loss rate escalated by 1 order of magnitude over the final decades, rising from $\sim$0.04 to $\sim$0.6 $M_\odot$ yr^{-1}. This surge produced a massive, extended CSM shell of $\sim 3\ M_\odot$ out to $\sim 3.5 \times 10^{16}$ cm. The young stellar environment ($\sim$100 Myr) together with this substantial, extensive CSM points to a progenitor system consisting of a white dwarf and an intermediate-mass companion that underwent increasing mass loss prior to explosion.

Unified Astronomy Thesaurus concepts: Supernovae (1668); Type Ia supernovae (1728); Circumstellar matter (241)

Materials only available in the online version of record: data behind figure

1. Introduction

Type Ia supernovae (SNe Ia) are fundamental tools for measuring cosmic distances and the expansion history of the Universe (A. G. Riess et al. 1998; S. Perlmutter et al. 1999). However, the nature of their progenitor systems remains unresolved. The two leading scenarios are the single-degenerate (SD) model, in which a carbon-oxygen white dwarf (WD) accretes matter from a nondegenerate companion until it approaches the Chandrasekhar mass ($M_{\rm Ch} \approx 1.4\,M_\odot$) and undergoes a thermonuclear explosion (Z. Han & P. Podsiadlowski 2004; B. Wang 2018), and the double-degenerate (DD) model, involving the merger of two WDs (R. Pakmor et al. 2013).

Observational clues to distinguish these channels are often ambiguous. While the general absence of circumstellar material (CSM) around most SNe Ia favors the DD scenario (D. C. Leonard 2007; J. S. Bloom et al. 2012), the detection of time-variable Na I D absorption lines in some events points to the presence of nonuniform CSM, consistent with residual material from an SD companion (F. Patat et al. 2007; A. Sternberg et al. 2011).

More direct evidence for preexplosion mass loss comes from SNe Ia that exhibit clear signatures of CSM interaction. SN 2002ic was the first case, displaying narrow Hα emission characteristic of shocked, dense CSM and establishing the Ia–CSM subclass (M. Hamuy et al. 2003; N. N. Chugai & L. R. Yungelson 2004; N. N. Chugai et al. 2004; J. Deng et al. 2004; L. Wang et al. 2004). The core-degenerate (CD) scenario, involving a WD merging with the core of an asymptotic giant branch (AGB) star, has also been proposed for such events (A. Kashi & N. Soker 2011; B. Wang et al. 2017). Subsequent discoveries, including SNe 2005gj (G. Aldering et al. 2006; J. L. Prieto et al. 2007), 2018evt (Y. Yang et al. 2023; L. Wang et al. 2024), and 2020uem (K. Uno et al. 2023a, 2023b), have further solidified this class, challenging pure DD models and underscoring the role of enriched circumstellar environments.

This persistent progenitor ambiguity complicates the use of SNe Ia as precision cosmological tools, as different explosion channels could systematically affect their luminosity calibration and, consequently, inferences about dark energy (D. A. Howell 2011). Discrepancies with binary population synthesis models add to the challenge of reconciling predicted and observed SN Ia rates (D. Maoz et al. 2014).

A key manifestation of SN Ia diversity is the wide range of observed peak luminosities. At the bright end of the Phillips relation (M. M. Phillips 1993), SN 1991T-like events (e.g., A. V. Filippenko et al. 1992; M. M. Phillips et al. 1992) are characterized by strong iron-group element (IGE) features and weak intermediate-mass element (IME) lines. Their high nickel yields (e.g., $\sim$1 $M_\odot$ for SNe 1991T and 2011hr; M. Sasdelli et al. 2014; J.-J. Zhang et al. 2016) likely result from efficient burning, yet remain consistent with the standard Chandrasekhar-mass regime (e.g., L. Hu et al. 2022; M. M. Phillips et al. 2024). A separate group of even more luminous "super-Chandrasekhar" (SC) candidates, such as SNe 2003fg, 2006gz, 2007if, and 2009dc, challenge this limit with inferred ejecta or nickel masses potentially exceeding $M_{\rm Ch}$ (D. A. Howell et al. 2006; M. Hicken et al. 2007; W. Hillebrandt et al. 2007; K. Maeda et al. 2009; M. Yamanaka et al. 2009; R. A. Scalzo et al. 2010; M. Tanaka et al. 2010; F. Yuan et al. 2010; J. M. Silverman et al. 2011; S. Taubenberger et al. 2011). Proposed channels for these extreme events include rapidly rotating SD progenitors (B. Wang et al. 2014) and massive DD mergers (D. Liu et al. 2018).

CSM interaction provides an additional pathway to extreme luminosity. In SNe Ia–CSM, the conversion of shock kinetic energy into radiation can augment or even dominate the power source. Some events with early iron-rich spectra plus strong interaction reach luminosities rivaling those of SC candidates (J. M. Silverman et al. 2013; Y. Sharma et al. 2023). Such objects are key to mapping progenitor channels, power sources, and potential cosmological systematics.

In this work, we present SN 2022erq, a superluminous ($M_r \approx -21$ mag) thermonuclear transient that exemplifies this regime. Its photospheric spectra are dominated by IGE lines accompanied by persistent narrow Hα emission from ongoing CSM interaction. Using Hα diagnostics and bolometric light-curve modeling, we characterize the CSM properties and reconstruct the preexplosion mass-loss history. We place SN 2022erq within the landscape of superluminous thermonuclear transients and argue that the observed diversity among such events is primarily governed by the presence and properties of CSM, which can dominate the observed energetics even when the underlying explosion produces a substantial mass of IGEs.

The paper is organized as follows. Section 2 describes the observations of SN 2022erq. Section 3 presents the multiband photometry. Section 4 presents the spectral evolution and diagnostics. Section 5 discusses the environment, bolometric luminosity, CSM properties, and progenitor system. Section 6 summarizes the main conclusions.

2. Observations

2.1. Discovery and Classification

SN 2022erq was discovered by the Asteroid Terrestrial-impact Last Alert System (ATLAS; J. Tonry et al. 2022) on 2022 March 11.59 (UTC dates are used throughout this work). A spectrum obtained on 2022 March 12.90 revealed narrow Balmer emission lines superposed on a continuum with broad iron-group absorption features, leading to its classification as an SN 2005gj-like event (L. Li et al. 2022).

This SN is located at R.A. = $18^{\rm h}33^{\rm m}25\overset{\rm s}{.}36$, decl. = $+44^\circ05'11\overset{''}{.}65$ (J2000), residing in a faint irregular dwarf galaxy. A redshift $z = 0.0653 \pm 0.0001$ is measured from narrow host-galaxy emission lines (e.g., [O III] $\lambda\lambda$4959, 5007; [S II] $\lambda\lambda$6716, 6731) present in late-time spectra. Adopting $H_0 = 73.04\,{\rm km\,s^{-1}\,Mpc^{-1}}$ (A. G. Riess et al. 2022), the corresponding distance is $D = 270 \pm 30$ Mpc.

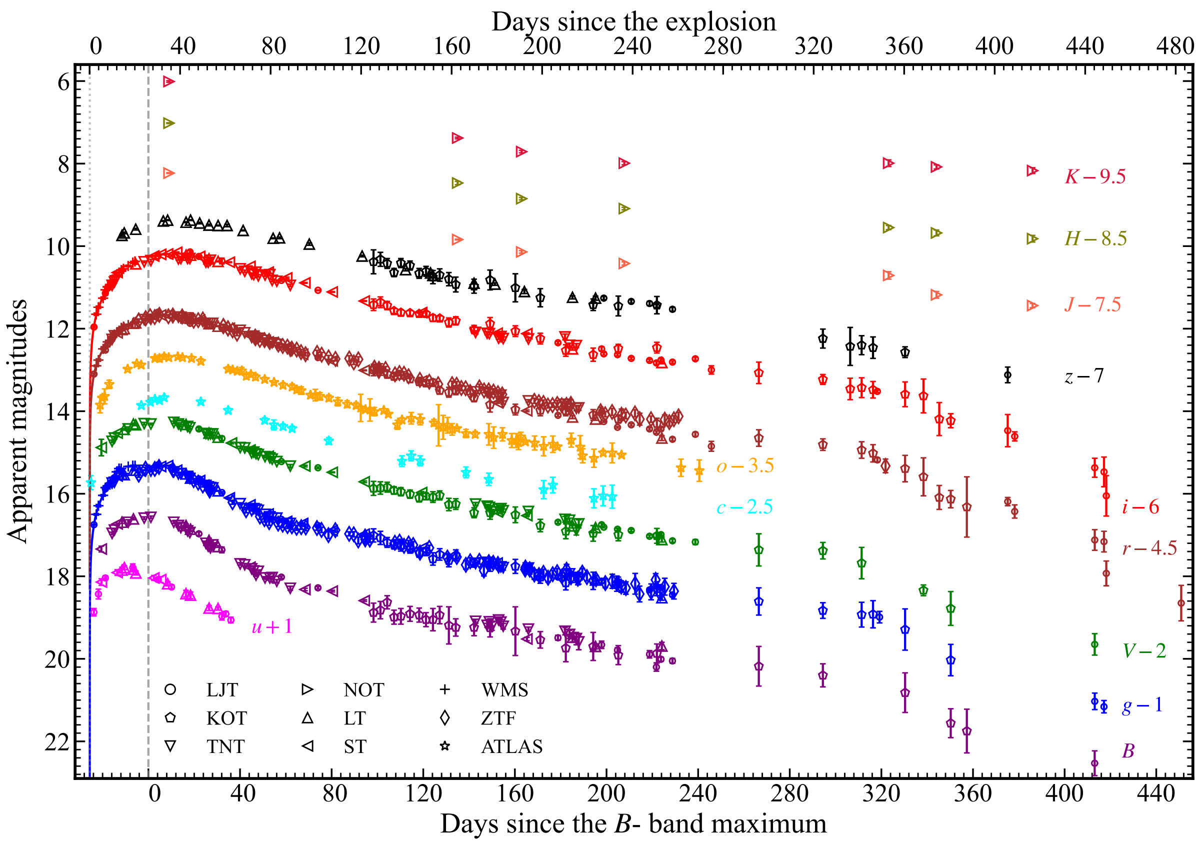

Figure 1. Optical and NIR light curves of SN 2022erq. Dotted and dashed vertical lines mark the explosion epoch and the time of *B*-band maximum, respectively. The data presented in this work are supplemented with public photometry from ZTF and ATLAS. The early time rise in the *gri* bands is fitted with a power-law (fireball) model.

2.2. Photometry

SN 2022erq was monitored extensively in the *BVugrizJHK* bands using a network of facilities (see Appendix A.1). For the optical *BVugriz* bands, host-galaxy subtraction was performed using template images. Specifically, the *griz* templates were constructed from preexplosion Pan-STARRS archival data. For the *u* and *BV* bands, template images were obtained in 2025 November, when the SN had faded sufficiently, and its spectrum showed virtually no remaining interaction signatures. Since the *u* and *BV* bands do not cover the Hα emission line, any residual CSM-interaction contribution in these templates is negligible. Point-spread-function (PSF) photometry was applied to the near-infrared (NIR) *JHK*-band data.

Figure A1 provides a finder chart for SN 2022erq and the local reference stars used for photometric calibration. The standardized magnitudes of these reference stars are listed in Table A1. They were calibrated using photometry from the Pan-STARRS catalog (*griz* bands; E. A. Magnier et al. 2020), the Two Micron All Sky Survey (*JHK* bands; M. F. Skrutskie et al. 2006), and observations of photometric standard stars (*BV* and *u* bands). Transformations from instrumental to standard magnitudes for the *BV* and *u* bands were derived on photometric nights using standard stars, e.g., Landolt standards for the *BV* bands (A. U. Landolt 1992) and Sloan Digital Sky Survey standard stars for the *u* band. For each filter, we solved for the photometric zero-points and color terms, and applied these transformations to the local sequence stars in the SN 2022erq field. The SN magnitudes were then obtained by differential photometry relative to these calibrated local standards and, where necessary, fine-tuned by enforcing consistency between repeated measurements and between overlapping datasets from different instruments. All instrumental magnitudes of SN 2022erq were calibrated against these local reference stars. The final, calibrated light curves are presented in Figure 1, with the complete photometric dataset provided in Tables A2 and A3. For comparison, we also plot publicly available Zwicky Transient Facility (ZTF[31]; E. C. Bellm et al. 2019; M. J. Graham et al. 2019) *gr*-band data and ATLAS[32] (J. L. Tonry et al. 2018; K. W. Smith et al. 2020) *c*- and *o*-band measurements obtained from forced photometry in Figure 1.

The last ATLAS nondetection in the *c* band occurred on 2022 March 9.66. Together with the subsequent ATLAS discovery on March 11.59 in the same band, this provides an initial constraint on the explosion epoch of MJD $= 59649.6 \pm 1.0$. We further refine the explosion epoch to MJD $= 59649.1 \pm 0.5$ by fitting the early time *gri*-band light-curve rise with a simple fireball model (Figure 1), which assumes a uniformly expanding photosphere with constant surface luminosity (W. D. Arnett 1982). This estimate is consistent with the ATLAS nondetection, and we therefore adopt MJD = 59649.1 as the reference explosion time hereafter.

2.3. Spectroscopy

With the explosion epoch established, the first spectrum of SN 2022erq was obtained at $\tau \approx 1.8$ days (where τ denotes days since explosion, and *t* refers to days after *B*-band

[31] https://alerce.online/object/ZTF22aadgsdi
[32] https://fallingstar-data.com/forcedphot/

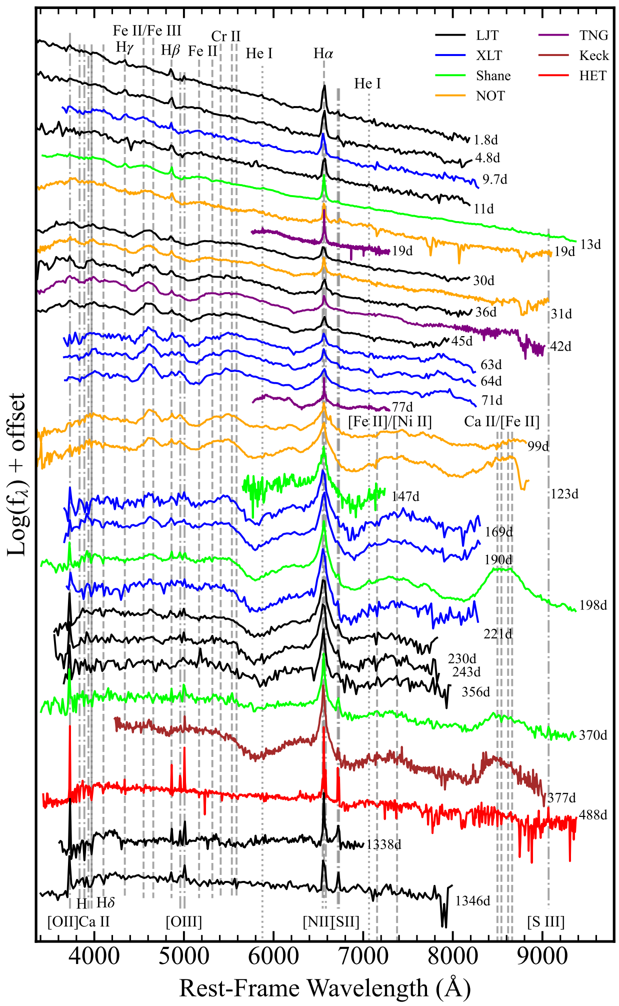

Figure 2. The spectral sequence of SN 2022erq. Epochs marked on the right side of each spectrum are relative to the adopted explosion date. Dashed and dotted lines mark the rest-frame wavelengths of features originating from the SN and the host galaxy, with identifications labeled above and below the spectrum, respectively. All spectra have been corrected for the host redshift and smoothed with bin sizes chosen according to the original signal-to-noise ratio.
(The data used to create this figure are available in the online article.)

maximum), making it the earliest spectroscopically confirmed SN Ia–CSM event. We conducted a spectroscopic campaign from $\tau \approx 2$ to 1350 days using multiple facilities (Appendix A.1). The spectral sequence is presented in Figures 2 and A3, with observational details provided in Table A4.

All spectra were processed with standard reduction pipelines, which included wavelength calibration, flux calibration, and correction for telluric absorption. The spectra were also shifted to the rest frame using the host-galaxy redshift. To minimize the effects of atmospheric dispersion, most observations were conducted with the spectrograph slit aligned at the parallactic angle (A. V. Filippenko 1982). For each spectrum, we then refined the flux scale and continuum shape using multiband photometry obtained at closely matching epochs.

For the subsequent analysis, all spectra were corrected for line-of-sight extinction. The absence of host-galaxy Na I D absorption indicates negligible host reddening, consistent with our environmental modeling (Section 5.1), which yields $A_V(\text{host}) \approx 0.046$ mag and $E(B - V)_{\text{host}} \approx 0.015$ mag (assuming $R_V = 3.1$). Including Milky Way reddening, $E(B - V)_{\text{MW}} = 0.0046 \pm 0.0005$ mag (E. F. Schlafly & D. P. Finkbeiner 2011), we adopt a total $E(B - V) = 0.02$ mag.

Table 1
Light-curve Parameters of SN 2022erq

Band	t_{max} (MJD)	t_{rise} (days)	m_{peak} (mag)	M_{peak} (mag)	Δm_{15} (mag)
u	59667.76	17.51	16.72	−20.51	0.38
B	59674.70	24.03	16.55	−20.67	0.23
g	59678.89	27.96	16.33	−20.89	0.22
V	59679.52	28.56	16.30	−20.90	0.19
r	59681.57	30.48	16.15	−21.05	0.15
i	59687.64	36.18	16.21	−20.98	0.11
z	59692.50	40.74	16.33	−20.85	0.10

Note. The rise time and the decline rates are calculated in the rest frame (corrected for the time-delay effect due to cosmological redshift). Typical uncertainties are <1 days for time measurements, 0.01–0.02 mag for apparent magnitudes and decline rates, and ∼0.1 mag for absolute magnitudes, dominated by the distance uncertainty.

3. Photometric Analysis

3.1. K-correction and Measurement

The observed *BVugriz*-band light curves of SN 2022erq were corrected for redshift-dependent effects using the K-correction method described in E. Y. Hsiao et al. (2007). For each photometric epoch, we applied a K-correction derived from a spectrum of SN 2022erq obtained at a similar phase. The resulting K-corrections as a function of time for each filter are shown in Figure A2. All subsequent light-curve analyses are based on these K-corrected data.

We measured light-curve parameters by fitting the K-corrected data with low-order polynomials. The resulting quantities, summarized in Table 1, include the peak time (t_{max}), rise time (t_{rise}), peak magnitude (m_{peak}), absolute magnitude (M_{peak}), and postmaximum decline of the light curve in 15 days (Δm_{15}).

Consistent with other Ia–CSM events, SN 2022erq shows a clear increase in the rise time from the blue to the red bands (J. L. Prieto et al. 2007; Y. Sharma et al. 2023). It reaches maximum light in the *u* band at $\tau \approx 17.5$ days, whereas the *z*-band peak occurs much later, at $\tau \approx 40.7$ days. This wavelength-dependent delay partially reflects the temperature evolution of the spectral energy distribution (SED), a common feature among most SNe. In SN 2022erq, however, the particularly slow evolution in the *r* band is further enhanced by the gradual strengthening of Hα emission, which contributes additional flux at this wavelength and prolongs the rise toward maximum.

The *JHK*-band light curves are more sparsely sampled. The earliest NIR epoch at $\tau \approx 34.6$ days likely precedes the true maxima, so the NIR peak magnitudes, estimated from the earliest data near maximum, should be regarded as lower limits: $M^J_{\text{peak}} \approx -21.45$, $M^H_{\text{peak}} \approx -21.65$, and $M^K_{\text{peak}} \approx -21.66$ mag.

3.2. Light Curve

The photometric parameters of SN 2022erq are summarized in Table 1. A comparison with normal SNe Ia, luminous 1991T-like events, and SC candidates (Table 2) demonstrates its extreme luminosity relative to these classes. At the peak, SN 2022erq is ∼ 1.5 mag brighter in the *B* band than a typical SN Ia. This excess increases to ∼2.5 mag by $t = +15$ days and

Table 2
B-band Light-curve Parameters

SN	t_{rise} (days)	M_{max} (mag)	Δm_{15} (mag)	Δm_{50} (mag)	z	References
2022erq	24.03	−20.67	0.23	1.42	0.0653	(1)
2011fe	17.26	−19.24	1.18	3.36	0.0012	(2)
1991T	17.90	−19.98	0.95	3.04	0.0058	(3)
2011hr	19.17	−19.84	0.93	3.03	0.0133	(4)
2007if	20.67	−20.53	0.76	2.77	0.0742	(5)
2009dc	21.83	−20.22	0.73	2.78	0.0216	(6)

Note. *B*-band light-curve parameters of SN 2022erq with those of normal SN Ia SN 2011fe, 91T-like (SN 1991T, SN 2011hr), and SC candidates (SN 2007if, SN 2009dc). The rise times and the decline rates are calculated in the rest frame (corrected for the time-delay effect due to cosmological redshift). References: (1) this work; (2) K. Zhang et al. (2016); (3) M. Sasdelli et al. (2014); (4) J.-J. Zhang et al. (2016); (5) R. A. Scalzo et al. (2010); (6) M. Tanaka et al. (2010).

to ∼3.5 mag by $t = +50$ days. The contrast is even stronger in the r band, consistent with enhanced longer-wavelength emission from the shocked CSM, e.g., Hα emission (Y. Sharma et al. 2023).

Figure 3 compares the multiband light curves of SN 2022erq with those of a broader sample, extending the comparison in Table 2 to include the Ia–CSM SN 2005gj and SN 2018evt, and the Type IIn SN 2010jl. SN 2022erq is slightly more luminous than SN 2005gj, but their light curves share a similar morphology. Both exhibit a slow rise and a gradual decline, a characteristic signature of early sustained CSM interaction that governs their photometric evolution. The CSM interaction in SN 2022erq appears to weaken at $t \gtrsim +330$ days, as indicated by a clear steepening of the decline rate in all bands.

SN 2018evt, in contrast, was fainter at early times, consistent with its weaker early time spectroscopic signatures of interaction. Although its late-time light curve indicates prolonged interaction, the lack of very early observations precludes a precise constraint on the onset of its CSM-interaction phase. When reobserved from $t \gtrsim +120$ days onward, SN 2018evt exhibited a luminosity comparable to SN 2022erq at B and g bands, and surpassed it after $t \gtrsim +200$ days. It evolved more slowly, with a sharp downturn after $t \gtrsim +500$ days. Given the spectral similarity of these two SNe at $\tau \sim$ 150–250 days (Section 4.2), which implies comparable ejecta velocities, the higher late-time luminosity and the delayed rapid decline of SN 2018evt indicate that its outer CSM is likely both denser (or more optically thick) and more spatially extended than that of SN 2022erq.

Figure 4 places SN 2022erq in a broader context by plotting peak *r*/*R*-band absolute magnitude against light-curve width (duration above half-maximum) for SNe Ia, including Ia–CSM events. SN 2022erq lies at the luminous extreme of this parameter space. The diversity in peak luminosity and light-curve evolution among these interacting transients results from differences in the onset strength of the SN–CSM interaction and in the efficiency of converting shock kinetic energy to radiation. SN 2022erq represents a case of exceptionally early and efficient coupling.

3.3. Color Curve

Figure 5 compares the $g - r$ color evolution of SN 2022erq with a sample of SNe Ia, including SNe Ia–CSM, and other well-studied transients. SN 2022erq closely tracks the evolution of luminous SNe Ia–CSM like SN 2005gj. With the very early coverage, SN 2022erq shows an initial blueward drift as the temperature rises, reaching the bluest $g - r$ color roughly 2 weeks before the r-band maximum, followed by a gradual reddening, which is a pattern broadly analogous to normal SNe Ia.

Around the maximum light, SN 2022erq is redder than normal SNe Ia. Its V-band peak is ∼0.2 mag brighter than its B-band peak, whereas in normal SNe Ia these two bands typically peak at a similar brightness (X. Wang et al. 2009). The relative redness is consistent with the finding that SNe Ia–CSM are generally cooler than normal SNe Ia at early times (Y. Sharma et al. 2023).

SN 2022erq reaches its reddest $g - r$ color at ∼50 days after the r-band maximum, with a value of ∼0.7 mag smaller than typical SNe Ia. The luminous SN 1991T and the SC candidate SN 2007if reach a comparable maximum $g - r$ colors to SN 2022erq.

Thereafter, the $g - r$ color of SN 2022erq and other Ia–CSM SNe evolves slowly, settling onto a plateau of ∼0.5 mag. This sustained plateau coincides in time with the formation and persistence of a cold dense shell (CDS) seen in the spectra (Section 5.2), and is likely maintained by ongoing CSM interaction (continuous energy input and possible obscuration). In contrast, the $g - r$ color of normal SNe Ia, SN 1991T, and SN 2007if declines rapidly after reaching its maximum, reflecting the absence of the sustained CSM-interaction phase that dominates the late-time emission.

The similarity in the color evolution between luminous SNe Ia–CSM like SN 2005gj and SN 2022erq may point to a common physical origin. However, not all SNe Ia–CSM follow this behavior. The subluminous Ia–CSM SN 2019ibk ($M^r_{max} \approx -17.5$ mag; Y. Sharma et al. 2023) remains significantly bluer within ∼120 days after r-band maximum, hinting at different progenitors, explosion mechanisms, CSM properties, or viewing angles. Besides, the Type IIn SN 2010jl is even redder than SNe Ia–CSM, likely due to stronger obscuration of the underlying SN by a denser, hydrogen-rich CSM.

4. Spectral Analysis

4.1. Evolution

The long-term spectroscopic campaign of SN 2022erq offers a rare opportunity to trace the evolution of an SN Ia–CSM. Its early time spectra are dominated by a narrow Hα emission. The origin of this feature, whether from the underlying host galaxy or from SN–CSM interaction, can be reliably diagnosed from its temporal evolution. Owing to the limited spectral resolution of our early data (instrumental full width at half-maximum, FWHM ≈ 700–1000 km s^{-1}), any truly narrow galactic component and a somewhat broader interaction-powered component would be blended, so the line width alone cannot be used as a robust discriminator. Instead, we rely on the evolution of the relative strength of the emission lines. The significantly weaker relative intensities of galactic emission lines (e.g., [S II], [N II], [O II], [O III]) with respect to Hα in the early spectra compared to the late-time spectra at $\tau \gtrsim 1300$ days when the SN has faded below the detection threshold indicate that the initial Hα and Hβ emission originate from SN–CSM interaction rather than galactic contamination.

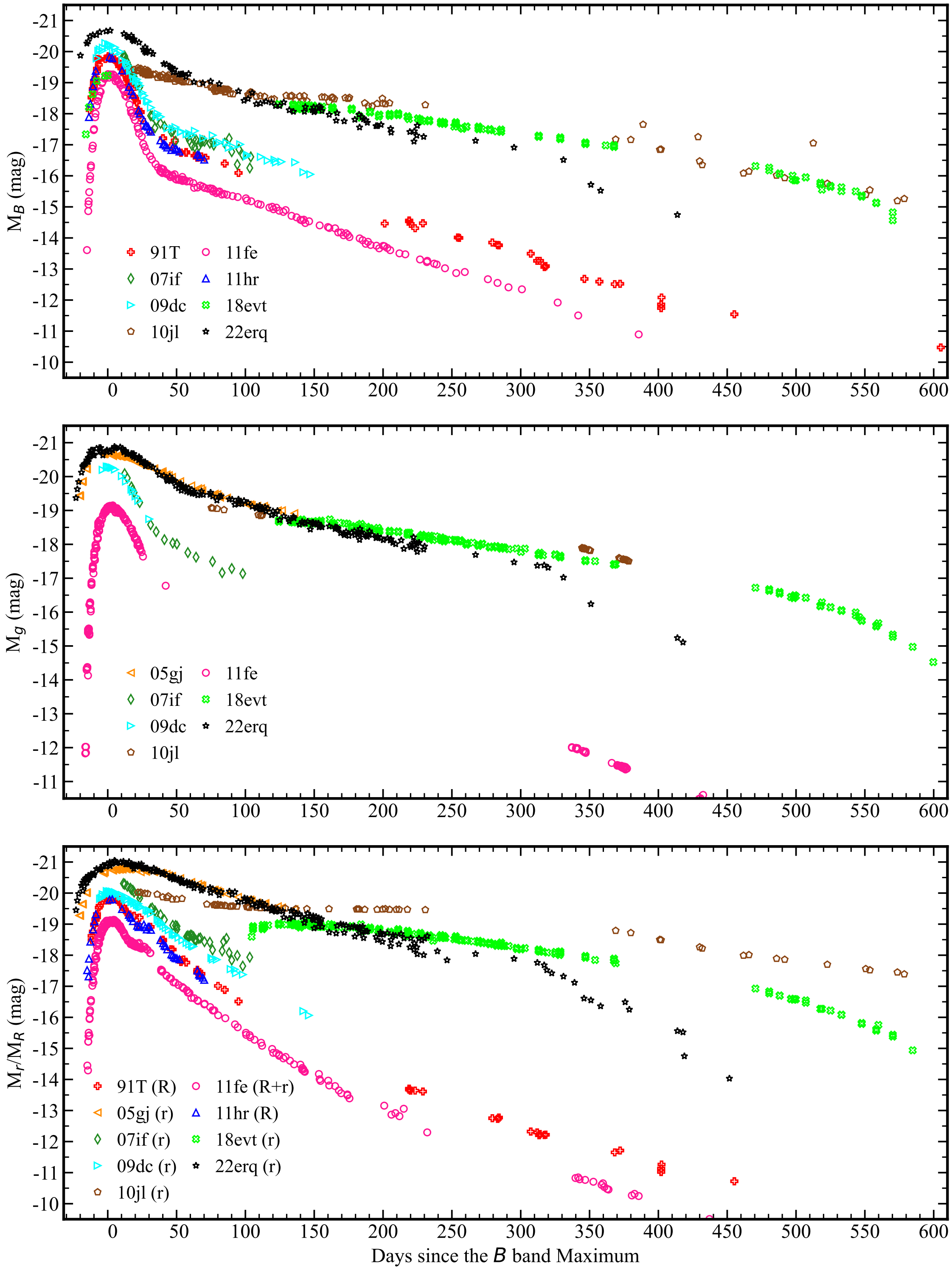

Figure 3. The *B*-, *g*-, and *r*/*R*-band light curves of SN 2022erq compared with representative events: SNe Ia–CSM (SNe 2005gj, 2018evt; G. Aldering et al. 2006; J. L. Prieto et al. 2007; Y. Yang et al. 2023; L. Wang et al. 2024), SC candidates (SNe 2007if, 2009dc; R. A. Scalzo et al. 2010; S. Taubenberger et al. 2011; M. Hicken et al. 2012; J. M. Silverman et al. 2012; B. E. Stahl et al. 2019), 91T-like SNe (SNe 1991T, 2011hr; A. V. Filippenko et al. 1992; M. M. Phillips et al. 1992; B. P. Schmidt et al. 1994; J.-J. Zhang et al. 2016), the normal SN Ia SN 2011fe (P. E. Nugent et al. 2011; U. Munari et al. 2013; R. E. Firth et al. 2015; K. Zhang et al. 2016), and the Type IIn SN 2010jl (R. Stoll et al. 2011; N. Smith et al. 2012; C. Fransson et al. 2014; E. O. Ofek et al. 2014). Where *r*-band coverage is insufficient or unavailable, *R*-band data are used as a complement or substitute.

Absorption from IMEs (e.g., Si, S, Ca) is nearly undetectable until near the time of the *B*-band maximum brightness (Figure 6). An emission bump at ∼4500 Å attributed to Fe II and Fe III emerges at $\tau \approx 20$ days, persists with stable strength until $\tau \approx 123$ days, and subsequently fades by $\tau \approx 170$ days. Additionally, a similar IGE-produced emission bump near 5500 Å, attributed to a blend of permitted lines of Cr II (e.g., $\lambda\lambda$ 5410, 5535, 5587) and Fe II λ 5316 (S. Blondin

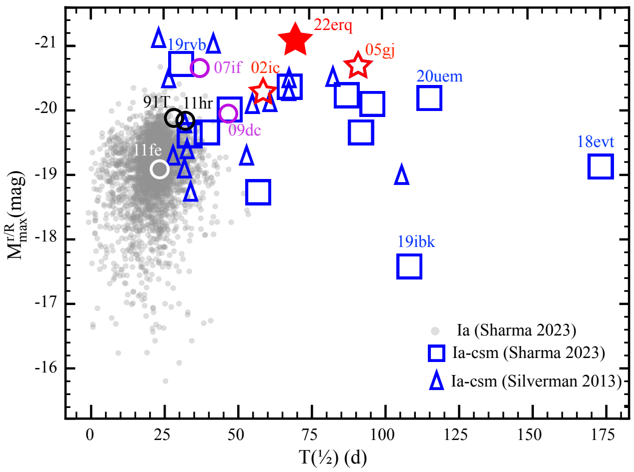

Figure 4. The peak *r/R*-band luminosity ($M_{max}^{r/R}$) versus duration above half-maximum luminosity ($T_{1/2}$) in the rest frame. The sample includes normal, 91T-like, SC candidate, and CSM-interaction SNe Ia from J. M. Silverman et al. (2013) and Y. Sharma et al. (2023).

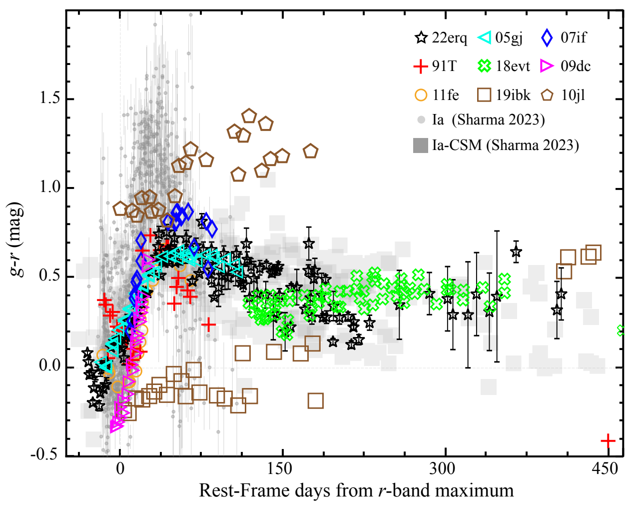

Figure 5. The $g - r$ color evolution of SN 2022erq compared to representative objects, including a sample of SNe Ia and Ia–CSM from Y. Sharma et al. (2023), as well as several other well-studied transients. All comparison objects have been corrected for reddening.

et al. 2015, 2018), becomes noticeable at $\tau \approx 60$ days, also fading by $\tau \approx 170$ days. Concurrently, the Hα line profile evolves slowly from $\tau \approx 100$ to 377 days.

At $\tau \approx 123$ days, two broad emission bumps appear near 7300 and 8500 Å. The former likely blends [Fe II] λ7155, [Ni II] λ7378, and [Fe II] λ 7720, while the latter may consist of the Ca II NIR triplet and [Fe II] λ8617. These features intensify and then weaken, remaining detectable at $\tau \approx 380$ days. Characteristic nebular-phase lines of normal SNe Ia, such as numerous Fe and Co emission lines in the blue, are absent in SN 2022erq, likely owing to CSM obscuration. At $\tau \approx 488$ days, all previously prominent SN features, including the broad Hα emission underlying the narrow component, have largely faded, and the spectrum becomes dominated by host-galaxy lines.

Overall, the spectroscopic evolution of SN 2022erq is notably slow, plausibly maintained by ongoing CSM interaction that converts shock kinetic energy into radiation and prolongs photospheric heating. This sustains high luminosity and delays spectral transitions, consistent with other interacting SNe (e.g., I. Arcavi et al. 2017; N. Smith 2017; J.-J. Zhang et al. 2020; Q. Zhai et al. 2025).

4.2. Comparison with Iron-rich SNe Ia

Spectroscopic identification of SN Ia–CSM events relies on the presence of multicomponent Hα emission (relatively narrow core with intermediate/broad base) superimposed on a diluted SN Ia spectrum, first established in SN 2002ic (M. Hamuy et al. 2003). Subsequent analyses indicated that the underlying SN component more closely resembles luminous, SN 1991T-like SNe Ia with enhanced IGE abundances (e.g., SNe 2005gj and 2018evt; G. Aldering et al. 2006; L. Wang et al. 2024).

Figure 7 compares SN 2022erq with spectroscopic templates of transients known for efficient nuclear burning: the luminous SNe 1991T and 2011hr, and the SC candidate SN 2007if (see Appendix A.2 for technical details). The aim of this comparison is to evaluate whether the photospheric signatures of SN 2022erq are consistent with an explosion that produced a high yield of IGEs. This task is challenging because strong CSM interaction boosts the continuum flux and can dilute photospheric absorption features.

In the first month, all comparison templates show broad agreement with SN 2022erq. The spectra are dominated by Fe II/Fe III absorption features near ∼10,000 km s^{-1}, while IME lines such as Si II λ6355 are exceedingly weak. This stands in stark contrast to normal SNe Ia such as SN 2011fe (Figure 6) and points to a common nucleosynthetic outcome characterized by efficient burning and a high IGE yield.

At later phases ($\tau \gtrsim 60$ days), detailed differences emerge. The spectrum of SN 2007if provides a close match across multiple epochs: the [Fe II] 5316-5535 Å quartet, the blended [Fe II]+[Ni II] complex near 7000-8000 Å, and the cleanly resolved lines [Fe II] λ7155, [Ni II] λ7378, and [Fe II] λ7720 at $\tau \approx 90$ days are all well reproduced. SN 1991T at a comparable epoch (∼59 days) also shows prominent Fe/Ni emission in this region, confirming a spectroscopic kinship; however, these features appear to fade more rapidly in SN 1991T than in SN 2022erq. SN 2011hr at ∼62 days matches SN 2022erq well at early times, but its spectral coverage ends too soon to assess the later evolution.

A definitive assessment of which individual object is the optimal match is limited by two factors. First, CSM interaction can significantly delay the spectroscopic evolution of the underlying SN, complicating direct phase-to-phase comparisons. Second, the available spectral sequences for the templates are incomplete and not perfectly aligned in time with the extensive coverage of SN 2022erq. Therefore, the comparison does not identify a unique genealogical link to a specific SN Ia subtype. Instead, it robustly establishes that the spectroscopic phenotype of SN 2022erq, marked by weak IMEs and strong, persistent IGE features, is shared with transients known to arise from highly efficient thermonuclear burning. This interpretation is supported by the low IME masses (e.g., ∼0.1–0.2 $M_\odot$) derived from detailed spectral modeling of SNe 1991T and 2011hr (M. Sasdelli et al. 2014; J.-J. Zhang et al. 2016).

We therefore conclude that the underlying explosion of SN 2022erq likely belongs to the same family of efficient-burning thermonuclear events as overluminous (SN 1991T-like) SNe Ia and some SC candidates (e.g., SN 2007if). Its position within this sequence is defined primarily by its

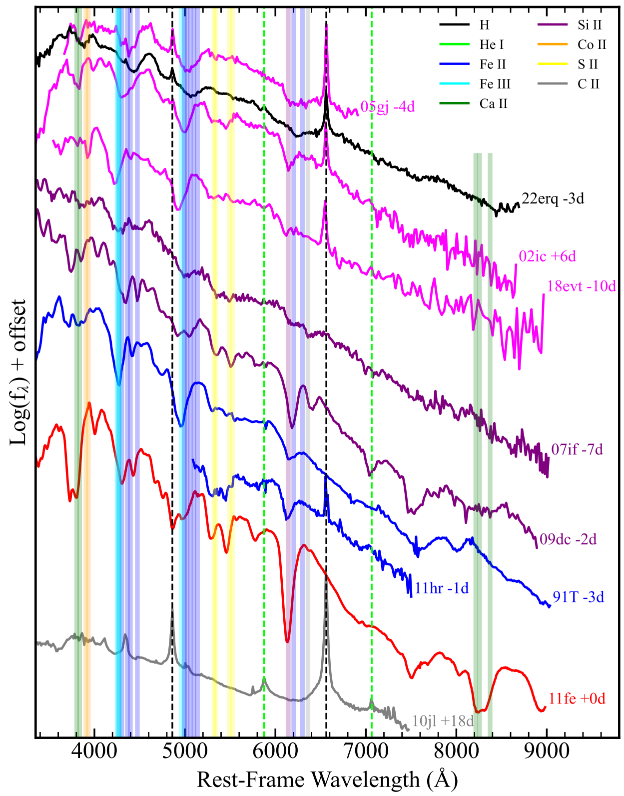

Figure 6. A spectral comparison of SN 2022erq near maximum brightness with SNe Ia–CSM (SNe 2002ic, 2005gj, 2018evt), SC candidates (SNe 2007if, 2009dc), 91T-like (SNe 1991T, 2011hr), normal SN Ia SN 2011fe (J. T. Parrent et al. 2012), and SN IIn SN 2010jl (N. Smith et al. 2012). Thin dotted lines mark rest-frame wavelengths; thick lines indicate features at a blueshift of 10,000 km s^{-1}. All spectra are dereddened.

nucleosynthetic yield. The subsequent analysis demonstrates that its extraordinary luminosity and light-curve behavior, however, are dictated not by this yield, but by the conversion of kinetic energy via interaction with its massive, hydrogen-rich CSM.

4.3. Comparison with Other CSM-interacting SNe

A comparison with other SNe Ia–CSM (Figure 8) shows that SN 2022erq most closely resembles SN 2005gj during the first year. The nearly identical spectroscopic evolution of SN 2022erq and SN 2005gj, together with the similarity with SN 2007if established above, suggests that SN 2007if may also serve as a useful spectral analog for SN 2005gj, a connection possibly overlooked because SN 2007if was discovered later. The interaction signatures in SN 2022erq begin to fade after $\tau \approx 380$ days, a timing that coincides with the clear steepening of the light-curve decline observed from $t \gtrsim +330$ days. This earlier weakening, compared with the prolonged interaction seen in SN 2018evt, implies that the CSM around SN 2022erq is less spatially extended. On the other hand, the stronger early time SN Ia signatures (e.g., more distinct IME absorptions) and the weaker Hα emission in SNe 2002ic and 2018evt correlate with their lower peak luminosities, indicating that CSM interaction was weaker at early phases in those events.

SN 2022erq differs fundamentally from SNe IIn in its CSM properties. Its high Balmer decrement (Hα/H$\beta \approx 7$), approximately double that of SN 2010jl at a comparable phase, aligns with other SNe Ia–CSM (Y. Sharma et al. 2023) and suggests enhanced continuum opacity or dust extinction. The asymmetric Hα profile ($\tau \gtrsim 100$ days), with a suppressed red wing, may indicate dust formation (L. Wang et al. 2024). The absence of Hγ emission, prominent in SN 2010jl (Figure 6), might point to a different ionization conditions or excitation states. While no clear reliable narrow optical He I emission is seen, a distinct P-Cygni profile in the He I λ10,830 line is present in all NIR spectra of SN 2022erq ($13 < \tau < 150$ days; Figure A3), confirming helium in the CSM and suggesting that the optical He I lines are suppressed due to higher optical depth or different ionization balance.

The comparison of the optical–NIR spectral properties of SN 2022erq with those of SNe 2018evt and 2010jl (Figure 9) highlights both shared and distinct characteristics. All three objects exhibit dominant H emission lines, including the Balmer, Paschen, and Brackett series. The Brackett series lines in SN 2022erq are weaker than in SN 2018evt and SN 2010jl, indicating similar CSM compositions but differing density and temperature. A spectral bump observed at ∼12,000 Å in SN 2022erq and SN 2018evt may originate from Mg I $\lambda\lambda$11,828, 12,047, which is less pronounced in SN 2010jl, suggesting differences in their inner SN compositions.

5. Discussion

5.1. Galactic Environment

Late-time spectra ($\tau \gtrsim 488$ days) of SN 2022erq are dominated by host-galaxy light. They show emission lines overlay Hβ and Hγ absorption, indicating contributions from ionized gas and a substantial stellar population. The spectrum at $\tau \approx 488$ days was selected for its high signal-to-noise ratio (S/N) and high resolution to probe the local environment. Applying the R23 index (H. A. Kobulnicky & L. J. Kewley 2004), defined as ([O II] λ3727 + [O III] $\lambda\lambda$4959, 5007)/Hβ, to this spectrum gives 12 + log(O/H) =8.45 ± 0.05, or ∼58% of the solar value (M. Asplund et al. 2009). This indicates a higher gas-phase metallicity for SN 2022erq than that of SN 2007if, derived with the same method (∼20% solar; M. Childress et al. 2011).

To characterize integrated stellar properties, we fit the host SED using Pan-STARRS *g*, *r*, *i*, *z* photometry and BayeSED3 (Y. Han et al. 2023). The modeling adopts G. Bruzual & S. Charlot (2003) single stellar population models, a Chabrier initial mass function, an exponentially declining star formation history, the D. Calzetti et al. (2000) dust-attenuation law, and nebular emission for populations younger than 10 Myr (N. Byler et al. 2017).

The SED fit constrains the stellar population age to $\log(t_{\rm age}/{\rm yr}) = 8.02^{+0.04}_{-0.02}$, corresponding to ∼105 Myr, indicating a relatively young stellar population. The stellar metallicity is constrained to $\log(Z/Z_\odot) = -2.13^{+0.16}_{-0.09}$, about 0.7% of the solar metallicity, typical of low-metallicity galaxies. The dust attenuation in the V band is $A_V = 0.046^{+0.08}_{-0.03}$ mag, indicating minimal dust obscuration. The stellar mass is $\log(M_\star/M_\odot) = 7.97^{+0.03}_{-0.04}$, corresponding to about $9.3 \times 10^7 M_\odot$, with an average star formation rate over the past 100 Myr of $\log({\rm SFR}_{100\,{\rm Myr}}/[M_\odot\,{\rm yr}^{-1}]) = -0.17^{+0.16}_{-0.37}$, or $\sim 0.67\,M_\odot\,{\rm yr}^{-1}$.

A comparison between the pure stellar spectrum from the best-fit SED model and the observed host spectrum (Figure 10) shows general agreement in Balmer and Ca II absorption. The prominent discrepancy lies in the strong gas emission lines (e.g., from O, S, N) present in the observation but not in the stellar population model. This highlights the different

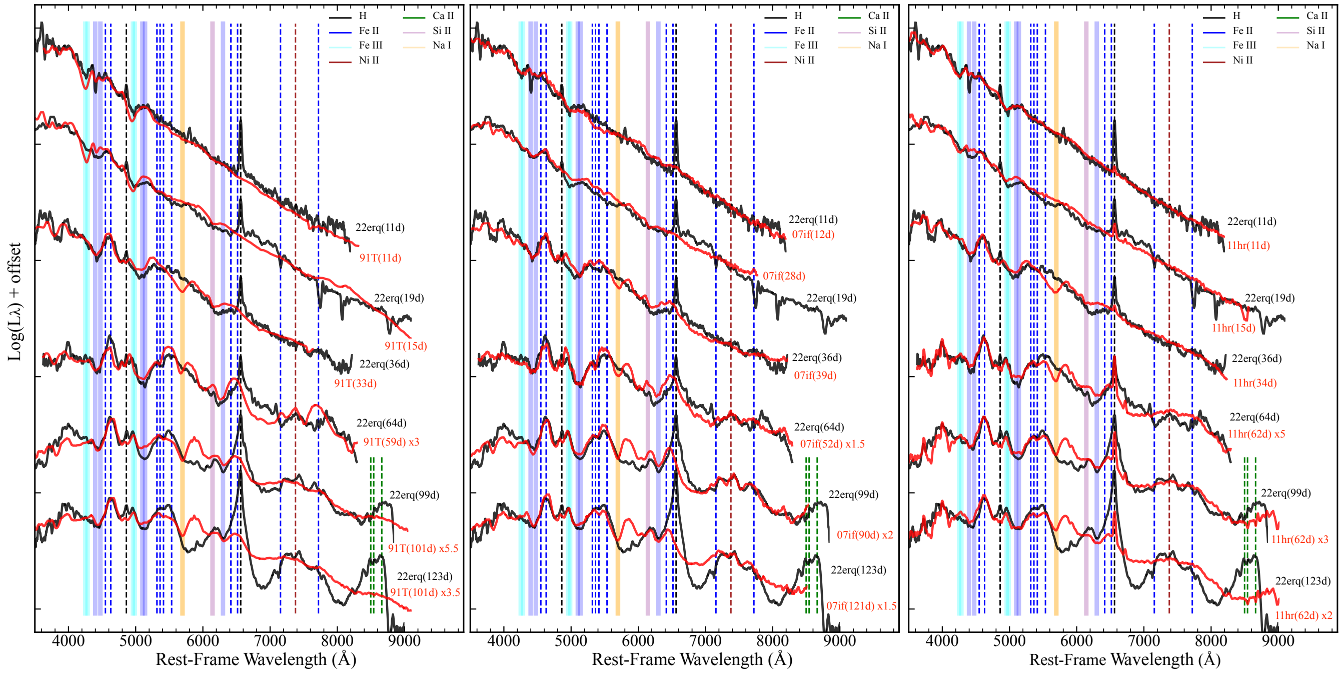

Figure 7. A spectral comparison of SN 2022erq with SNe 1991T, 2007if, and 2011hr. Luminosity scaling factors, where applied, are noted after the phase. Thin dotted lines indicate the rest-frame wavelengths of spectral lines, while thick lines show their positions at a blueshift of 10,000 km s^{-1}.

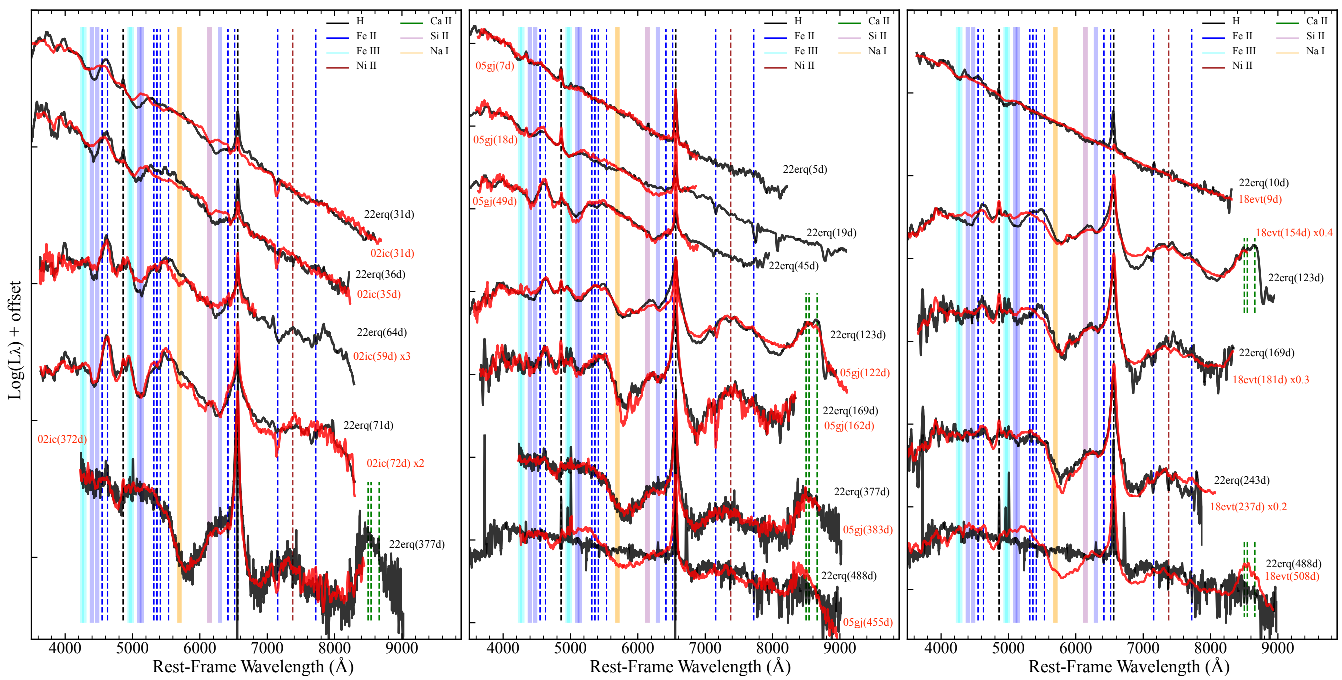

Figure 8. SN 2022erq compared with SN Ia–CSM SNe 2002ic, 2005gj, and 2018evt, following the same matching procedure applied in Figure 7.

astrophysical origins of the two metallicity estimates: the R23 index probes the present-day, gas-phase metallicity, while the SED-derived value represents the average metallicity of the stellar population. Such a disparity, where recently enriched gas is more metal rich than the older stellar bulk, is plausible in dwarf galaxies with recent star formation (L. van Zee & M. P. Haynes 2006; K. Nomoto et al. 2013; Y. Sharma et al. 2023).

These results show that SN 2022erq resides in a low-luminosity, star-forming, dwarf galaxy with subsolar metallicity. This environmental profile is consistent with the established properties of SNe Ia–CSM host galaxies (J. L. Prieto et al. 2007; J. M. Silverman et al. 2013).

5.2. CSM Properties from the Hα Emission

The evolution of the Hα profile provides a direct probe of the CSM properties and the interaction dynamics. Initially, the limited spectral resolution blends the instrumentally broadened narrow Hα line with a weak, underlying broader component.

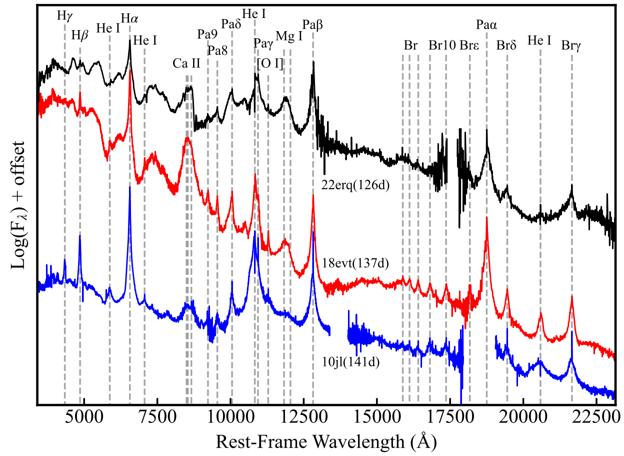

Figure 9. A phase-averaged spectrum of SN 2022erq at $\tau \approx 126$ days, constructed from adjacent optical and NIR observations, is compared with those of SNe 2018evt and 2010jl (T. Zhang et al. 2012; H. J. Borish et al. 2015). Dashed lines indicate the rest-frame wavelengths of the spectral lines.

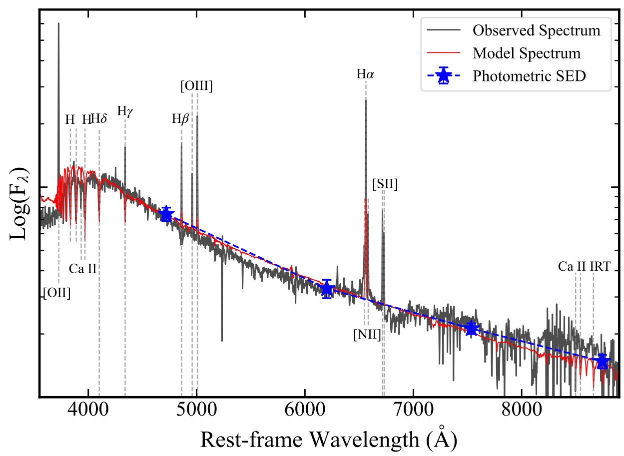

Figure 10. A comparison of the preexplosion host-galaxy photometric SED, the SED-derived model spectrum of the stellar population, and the late-time spectrum of SN 2022erq at $\tau \approx 488$ days (continuum corrected to match the host SED). Dashed lines mark rest-frame wavelengths of spectral lines.

As a result, the profile appears as a single feature, and the broad base is difficult to discern. At $\tau \approx 19$ days (Figure 11), improved resolution clearly decomposes the line into a narrow component ($\sim$200 km s^{-1}) from ionized, unshocked CSM, and an intermediate component ($\sim$2000 km s^{-1}), likely due to electron scattering (N. N. Chugai 2001). The FWHM of the narrow component is still close to the instrumental broadening, indicating a smaller intrinsic width (i.e., $\sim$100 km s^{-1} after the instrumental FWHM correction).

A distinct P-Cygni profile emerges by $\tau \approx 77$ days (Figure 11). The velocity shift of its absorption minimum indicates a CSM wind velocity of $\sim$180 km s^{-1}. The broad component further separates into an intermediate-width feature (FWHM $\approx$ 2000 km s^{-1}) and a very broad component (FWHM $\approx$ 5400 km s^{-1}) arising from the CDS formed between the forward and reverse shocks (N. N. Chugai 2001). The FWHM of this CDS component in SN 2022erq is significantly smaller than in SNe IIn (15,000–20,000 km s^{-1}; M. Stritzinger et al. 2012) but consistent with other SNe Ia–CSM (e.g., SNe 2005gj, 2018evt), suggesting systematically different CSM density distributions.

The NIR spectral evolution corroborates the findings from Hα. Both the He I λ10,830 line and the Paschen lines develop P-Cygni profiles with velocity separations similar to Hα (Figure 12), and all eventually show broad underlying components with comparable widths (Figure 11), indicating a common emitting region. A key difference is the earlier emergence ($\tau \approx 13$ days) of the narrow absorption component in the He I line compared to the hydrogen lines. This suggests that helium is more susceptible to resonance scattering, leading to detectable absorption features at earlier phases.

The mass-loss rate can be estimated from the narrow Hα luminosity ($L_{\mathrm{H}\alpha}$), using $L_{\mathrm{H}\alpha} \approx 2 \times 10^{39}\, \dot{M}_{0.01}^{2}\, v_{\mathrm{w},500}^{-2}\, \beta\, (r/10^{15}\ \mathrm{cm})^{-1}$ erg s^{-1} (E. O. Ofek et al. 2013), which assumes a wind-density profile and recombination-dominated Hα emission. Since the narrow Hα emission arises from unshocked, photoionized CSM ahead of the forward shock, it mainly probes the outer CSM and thus mass loss at earlier preexplosion epochs.

Adopting a wind velocity of 180 km s^{-1} and the host-subtracted $L_{\mathrm{H}\alpha}$ measured at $\tau \approx 19$ and 77 days, we derive mass-loss rates of 4.5×10^{-2} and $3.7 \times 10^{-2}\, M_\odot$ yr^{-1} for SN 2022erq, respectively, with an average value of $(4.1 \pm 0.4) \times 10^{-2}\, M_\odot$ yr^{-1}. This rate is intermediate compared to other SN Ia–CSM progenitors using an identical methodology (M. J. Childress et al. 2013; Y. Sharma et al. 2023).

With interaction persisting for $\sim$400 days and an ejecta velocity of 10,000 km s^{-1} derived from IGE absorption velocities, the CSM extends to $\sim 3.5 \times 10^{16}$ cm. A steady wind of 180 km s^{-1} would require $\sim$60 yr to build this shell. Combining this timescale with the average mass-loss rate derived from Hα ($\dot{M} \approx 0.04\, M_\odot$ yr^{-1}) yields a total CSM mass of $\sim 2.4\, M_\odot$ for a spherical geometry (or less if the CSM is aspherical or clumpy).

5.3. CSM Properties from Bolometry

The narrow Hα emission originates from the outer, cool, and tenuous CSM, and its analysis yields the mass-loss rate at earlier epochs (several decades before the explosion). Meanwhile, the postpeak evolution of the bolometric luminosity reflects the CSM density in the interaction region, i.e., the density at the location of the CDS formed by the ejecta–CSM interaction (R. A. Chevalier & C. Fransson 1994; W. M. Wood-Vasey et al. 2004; T. J. Moriya et al. 2013). Therefore, the CSM density derived from the bolometric light curve, together with that obtained from the Hα emission, can jointly depict a more complete picture of the CSM density structure.

Figure 13 shows the bolometric light curve of SN 2022erq, derived from blackbody fits to the observed SED spanning the *u*-*K* bands. Light curves in individual filters were interpolated onto a common time grid, and blackbody fits were performed only when at least four filters had detections; no extrapolation was applied to epochs with missing bands. The figure also shows quasi-bolometric luminosities from direct flux integration over *uBgVriz* and *uBgVrizJHK*. Although *u*-band data are unavailable for $t \gtrsim 40$ days, its contribution to the total luminosity is negligible at these epochs.

SN 2022erq reaches a peak bolometric luminosity of $L_{\mathrm{peak}} \approx 8 \times 10^{43}$ erg s^{-1} at $\sim$30 days after explosion, nearly an order of magnitude above typical SNe Ia. Applying Arnett's

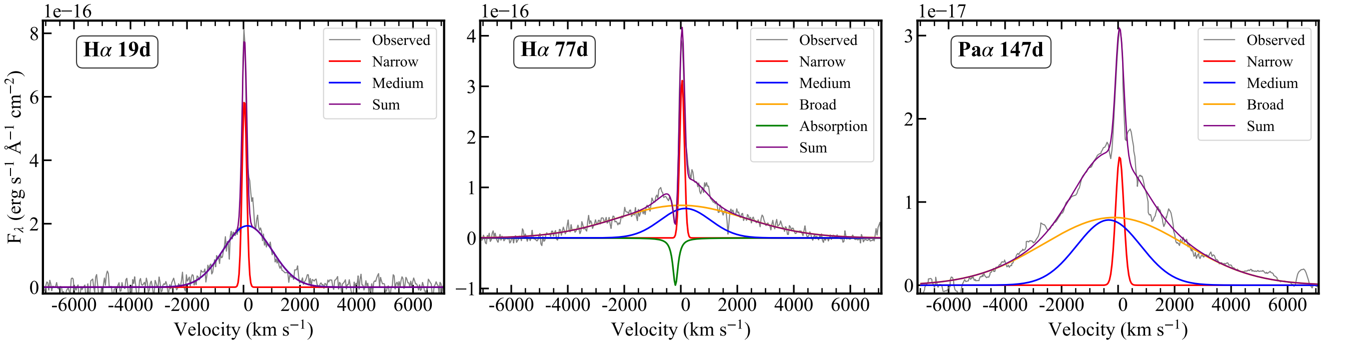

Figure 11. Multi-Gaussian fits to the Hα and Paα lines of SN 2022erq. The spectra with higher spectral resolution and S/N were selected to enable a robust decomposition of the line profiles. The instrumental FWHM is $\sim$210 km s^{-1} for the optical spectra and $\sim$150 km s^{-1} for the NIR spectrum.

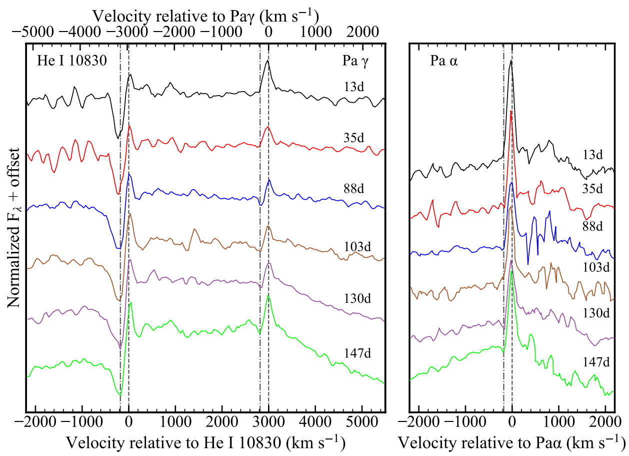

Figure 12. Spectral features normalized and displayed in the velocity space at selected phases. The left panel shows the He I λ10, 830 and Paγ lines, while the right panel presents the Paα line. Vertical lines indicate velocities of 0 km s^{-1} (dashed) and -180 km s^{-1} (dashed–dotted) relative to the host galaxy.

law (W. D. Arnett 1982; M. Stritzinger & B. Leibundgut 2005) to this luminosity and rise time would require an implausible ^{56}Ni mass of $M_{\rm Ni} \approx 6\,M_\odot$ for a thermonuclear SN, ruling out ^{56}Ni decay as the dominant power source. The slow postpeak decline and clear spectroscopic signs of interaction instead indicate that shock interaction with dense CSM is powering the light curve.

In this interaction-powered picture, the kinetic energy dissipated at the forward shock is

$$dE_{\rm kin} = 4\pi r_{\rm sh}^2\,\frac{1}{2}\rho_{\rm CSM} v_{\rm sh}^2\, dr_{\rm sh}, \tag{1}$$

so that the bolometric luminosity can be written as

$$L = \varepsilon\frac{dE_{\rm kin}}{dt} = 2\pi\varepsilon\ \rho_{\rm CSM}\ r_{\rm sh}^2 v_{\rm sh}^3, \tag{2}$$

where ε is the kinetic-to-radiative conversion efficiency, and $v_{\rm sh}$ is the velocity of the CDS.

Assuming canonical ejecta parameters for a Chandrasekhar-mass SN Ia ($M_{\rm ej} \sim 1.4\,M_\odot$, $v \sim 10^4$ km s^{-1}), the total shock kinetic energy is $\sim$1.4 foe. The total radiated energy obtained by integrating the bolometric light curve is $\sim$0.7 foe, which implies $\varepsilon \approx 50\%$. The CDS velocity $v_{\rm sh}(t)$ is measured from the FWHM of the broad Hα component: $v_{\rm sh} \approx 5400$ km s^{-1} at $\tau \approx 77$ days and 5900 km s^{-1} at $\tau \approx 147$ days (Figure 11), which can be parameterized as $v_{\rm sh}(t) = v_1\, t_d^{0.15}$, where t_d is the time in days since explosion, and $v_1 = 2800$ km s^{-1}. The shock radius $r_{\rm sh}(t)$ is then obtained by integrating $v_{\rm sh}(t)$ over time.

With $L(t)$, $v_{\rm sh}(t)$, and $r_{\rm sh}(t)$, we can invert the above relation to derive the CSM density $\rho_{\rm CSM}(r)$. The interaction-dominated phase begins at $\tau \approx 40$ days, when the luminosity has passed its peak and started to decline while remaining about an order of magnitude above a typical SN Ia, and when a pronounced CDS component appears in the spectra. The interaction-dominated phase is taken to end when the shock reaches the inner ejecta, corresponding to the rapid decline of the light curve at $\tau \approx 330$ days. The inferred CSM densities are shown as red stars in Figure 14. The CSM traced by the density profile extends from $\sim 1.5 \times 10^{15}$ cm to $\sim 1.6 \times 10^{16}$ cm, corresponding to a total CSM mass of $\sim 3.0\ M_\odot$. For comparison, independent density estimates derived from the narrow Hα emission are also plotted in Figure 14, constraining the outer CSM properties. The two sets of measurements are broadly consistent, both indicating a decreasing density at larger radii (i.e., at earlier epochs).

A power-law fit to these numerical results yields $\rho_{\rm CSM} \propto r^{-3.66}$. As an independent check, we fit the postpeak bolometric luminosity with $L \propto t^\alpha$, obtaining $\alpha = -1.46$. Using the analytic model of T. J. Moriya et al. (2013), the CSM density is parameterized as $\rho_{\rm CSM} \propto r^{-s}$, and the light-curve slope is related to the CSM density exponent s by $\alpha = \frac{6s - 15 + 2n - ns}{n - s}$, where $n \simeq 10$ is expected for SN Ia ejecta (C. D. Matzner & C. F. McKee 1999; D. Kasen 2010). From this, we derive $s = 3.59$, corresponding to $\rho_{\rm CSM} \propto r^{-3.59}$, in good agreement with the numerical result.

For a steady wind with a constant mass-loss rate and wind velocity $v_{\rm wind}$, the density profile is $\rho = \dot{M}/(4\pi r^2 v_{\rm wind})$, i.e., $\rho_{\rm CSM} \propto r^{-2}$. Taking $v_{\rm wind} = 180$ km s^{-1} (as derived in Section 5.2), this steady-wind behavior is illustrated by the colored dashed lines in Figure 14. Compared with a steady wind, the much steeper density profile of SN 2022erq implies a faster decline of density with radius, suggesting that the progenitor lost increasingly more material as it approached explosion. Starting about 20 yr before explosion, the mass-loss rate reached $\sim 0.04\ M_\odot$ yr^{-1}, increased to $\sim 0.1\ M_\odot$ yr^{-1} around 10 yr before explosion, and rose further to $\sim 0.25\ M_\odot$ yr^{-1} about 5 yr prior. In the final $\sim$3 yr, it escalated to an extraordinary $\sim 0.6\ M_\odot$ yr^{-1}. This trend indicates a dramatic enhancement of mass loss as the system approached explosion. These timescales are derived assuming a constant wind speed; if the outflow velocity evolved with time, the absolute timing would change, and the values quoted here should be regarded as approximate.

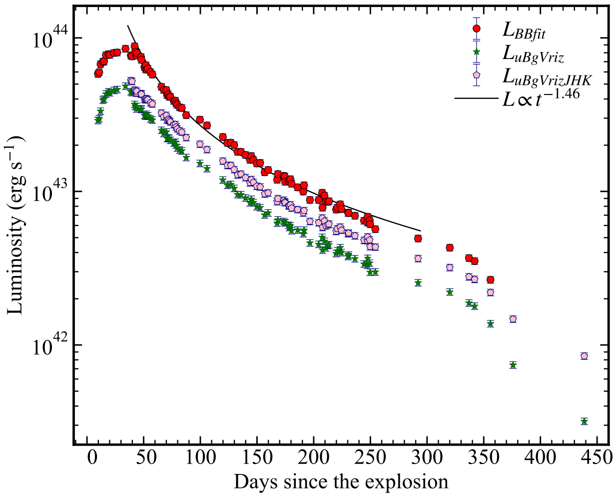

Figure 13. The bolometric light curve of SN 2022erq. Bolometric luminosities derived from blackbody fits to the observed SED are shown together with two sets of quasi-bolometric luminosities obtained by direct flux integration over the *uBgVriz* and *uBgVrizJHK* bands, respectively. The solid line represents the time-dependent power-law fit $L \propto t^{\alpha}$ to the postpeak light curve.

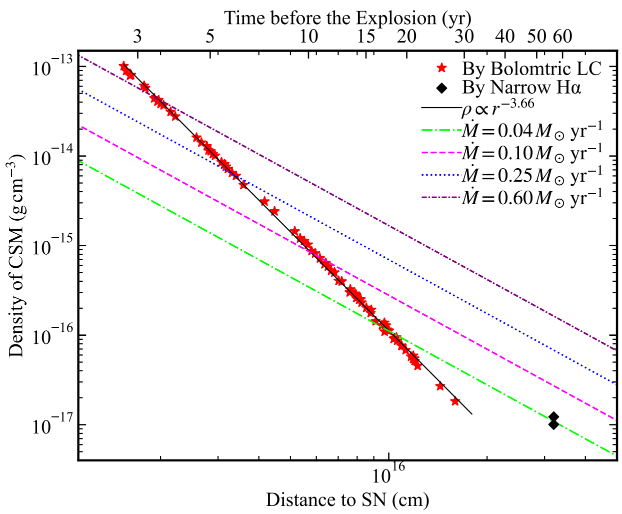

Figure 14. The CSM density profile of SN 2022erq. Red stars show densities inferred from the bolometric light curve, with a power-law fit $\rho_{\rm CSM} \propto r^{-s}$ (black line). Black diamonds mark independent density estimates from the narrow Hα line flux. Colored dash/dotted curves show steady-wind profiles $\rho = \dot{M}/(4\pi r^2 v_{\rm wind})$ for different mass-loss rates, assuming a constant wind velocity $v_{\rm wind} = 180$ km s^{-1}. The top axis gives the corresponding time before the explosion, $t = r/v_{\rm wind}$.

5.4. Progenitor System

The properties of SN 2022erq indicate a thermonuclear explosion inside a massive hydrogen-rich CSM. The inferred preexplosion mass-loss rate ($\sim$0.04–0.6 $M_\odot$ yr^{-1} over decades) exceeds by orders of magnitude the steady rates predicted by conventional SD models ($\sim 10^{-5}$–10^{-4} $M_\odot$ yr^{-1}; e.g., I. Hachisu et al. 1999; X. Meng et al. 2009). Nevertheless, the presence of such a massive hydrogen-rich CSM points to a progenitor with a nondegenerate companion, most likely an AGB star or a moderate-mass main-sequence star, consistent with enhanced-accretion scenarios for dense CSM formation (Z. Han & P. Podsiadlowski 2006). However, even the common-envelope wind (CEW) model (X. Meng & P. Podsiadlowski 2018) and the CD scenario (N. Soker 2011; B. Wang et al. 2017), which allow larger CSM reservoirs ($\sim$0.1–2 $M_\odot$), still marginally fall short of the $\sim$3 $M_\odot$ of CSM inferred for SN 2022erq, and it remains challenging for these models to naturally produce mass-loss rates as extreme as $\sim$0.6 $M_\odot$ yr^{-1}. Instead, this high rate likely requires a brief, violent ejection episode shortly before explosion, for example a delayed dynamical instability in the CEW framework (see Figure 2 in X. Meng & P. Podsiadlowski 2018) or a violent prompt merger in the CD scenario.

The young host environment and extensive CSM of SN 2022erq further support a short progenitor evolutionary timescale with substantial mass loss, consistent with a close binary that experienced a brief, high-mass-transfer phase immediately before explosion. The donor could be an intermediate-mass star ($\sim$3–7 $M_\odot$) undergoing rapid Roche-lobe overflow or incipient common-envelope evolution, although a lower-mass companion (for example, an AGB or red giant star) entering a dynamically unstable phase is also plausible. The short delay time implied by the young host also aligns with CD scenarios in which a WD rapidly merges with the core of a giant companion (B. Wang et al. 2017), although this channel faces additional constraints on retaining hydrogen-rich material.

6. Summary

SN 2022erq is the earliest confirmed member of the rare Ia–CSM class, a superluminous thermonuclear transient displaying clear circumstellar interaction signatures within 2 days of explosion. Through a combined analysis of early time spectroscopy and densely sampled photometry, this work shows that its extraordinary properties are driven by a massive, extended, hydrogen-rich CSM.

Photometrically, SN 2022erq reached a peak bolometric luminosity of $L_{\rm peak} \approx 8 \times 10^{43}$ erg s^{-1}, exceeding that of normal SNe Ia by roughly an order of magnitude. This extreme luminosity, together with its exceptionally slow postpeak decline, points to a dominant energy source beyond radioactive decay.

Spectroscopically, the early phases are dominated by IGEs with weak IME features, overlaid with persistent Hα emission from CSM interaction. At later epochs, the emergence and long-lived presence of a broad Hα component indicate sustained shock interaction and the formation of a CDS, which is also accompanied by a plateau in the color curve. In particular, the progressive strengthening of the Hα flux relative to the continuum contributes additional flux in the r band and helps to keep the $g - r$ color relatively red, rather than reflecting an intrinsic trend of the SED becoming redder.

These observations indicate that SN 2022erq arose from a highly efficient thermonuclear explosion embedded in an exceptionally massive, hydrogen-rich CSM. The IGE-rich, IME-weak spectrum points to efficient burning broadly similar to that inferred for some overluminous SNe Ia, while the peak and sustained superluminous output far exceeds what can be powered by radioactive decay alone. Instead, the light-curve morphology, color evolution, and Hα diagnostics together show that the observed radiation is overwhelmingly powered by ejecta–CSM shock interaction. In this picture, the extraordinary luminosity of SN 2022erq is a direct consequence of the efficient conversion of mechanical energy into radiation within the dense CSM, rather than a fundamentally different explosion mechanism.

An analysis of the Hα profile reveals a preexplosion mass-loss history characterized by a wind velocity of $\sim$180 km s^{-1} and a rate of $\sim$0.04 $M_{\odot}$ yr^{-1} sustained for $\sim$60 yr, producing a $\sim$2.4 $M_{\odot}$ CSM shell extending to $\sim$3.5 $\times$ 10^{16} cm. The bolometric light curve further constrains the evolution of the mass loss in the final decades before explosion, indicating that the mass-loss rate increased by an order of magnitude, from $\sim$0.04 to $\sim$0.6 $M_{\odot}$ yr^{-1} as the system approached explosion. Integrating the CSM density profile inferred from the bolometric light curve yields a total CSM mass of $\sim$3.0 $M_{\odot}$. The two mass estimates are broadly consistent. The lower value from Hα is expected, as it primarily traces the outer, ionized CSM under the assumption of a constant mass-loss rate, while the bolometric modeling probes the denser inner CSM and thus likely provides a more accurate measure of the total CSM mass.

SN 2022erq therefore demonstrates that understanding extreme thermonuclear transients requires disentangling the progenitor's explosion mechanism from its preexplosion mass-loss history. The escalation of mass loss in the final decades places strong constraints on the progenitor system and its late-stage evolution. In summary, the combined constraints—a massive hydrogen-rich CSM formed on decade-to-century timescales, a luminous thermonuclear event, and a young host environment—favor a close-binary progenitor that underwent a short-lived, high-mass-loss episode immediately before explosion. The most natural interpretation involves a near-Chandrasekhar-mass WD and a nondegenerate companion of intermediate mass, consistent with the mass-transfer and ejection timescales inferred from the CSM. This picture challenges steady-wind SD models and highlights the need for further theoretical and observational work on short-timescale, interaction-driven progenitor channels. Future high-cadence, high-resolution spectroscopy ($R \gtrsim 5000$), complemented by polarimetry and multiwavelength campaigns, will be essential for constraining the CSM geometry, explosion asymmetry, and progenitor nature in such strongly interacting systems.

Acknowledgments

This work is supported by the National Key R&D Program of China with grant 2021YFA1600404, the B-type Strategic Priority Program of the Chinese Academy of Sciences (grant XDB1160202), the National Natural Science Foundation of China (NSFC grants 12173082, 12333008, and 12225304), the Yunnan Fundamental Research Projects (YFRP grants 202501AV070012, 202401BC070007, 202501AS070005, and 202605AS350010), the Top-notch Young Talents Program of Yunnan Province, the Light of West China Program provided by the Chinese Academy of Sciences, the Yunnan Revitalization Talent Support Program (Yunling Scholar Project), and the International Centre of Supernovae, Yunnan Key Laboratory (grant 202302AN360001). X.W. is supported by the NSFC (grants 12288102, 12033003, and 11633002) and the Tencent Xplorer Prize. A.V.F.'s research group at U.C. Berkeley acknowledges financial assistance from the Christopher R. Redlich Fund, as well as donations from Gary and Cynthia Bengier, Clark and Sharon Winslow, Alan Eustace and Kathy Kwan, Timothy and Melissa Draper, Briggs and Kathleen Wood, Ellyn and Alan Seelenfreund (W.Z. is a Bengier-Winslow-Eustace Specialist in Astronomy; T.G.B. is a Draper-Wood-Seelenfreund Specialist in Astronomy), and numerous other donors. Y.C. is supported by the NSFC (grant No. 12303054), the Yunnan Fundamental Research Projects (grant Nos. 202401AU070063, 202501AS070078), the National Key Research and Development Program of China (grant No. 2024YFA1611603). Y.C. also acknowledges financial support from the SOXS project (PI S. Campana).

A.P., A.R., N.E.R., and G.V. acknowledge support from the PRIN-INAF 2022, "Shedding light on the nature of gap transients: from the observations to the models." A.R. also acknowledges financial support from the GRAWITA Large Program Grant (PI P. D'Avanzo). N.E.R. also acknowledges support from the Spanish Ministerio de Ciencia e Innovación (MCIN) and the Agencia Estatal de Investigación (AEI) 10.13039/501100011033 under the program Unidad de Excelencia María de Maeztu CEX2020-001058-M. J.V. is supported by the Hungarian NKFIH-OTKA grant K142534. The operation of the RC 80 telescope at Konkoly is based on the GINOP 2.3.2-15-2016-00033 grant funded by the European Union. C.P.G. acknowledges financial support from the Secretary of Universities and Research (Government of Catalonia) and by the Horizon 2020 Research and Innovation Programme of the European Union under the Marie Skłodowska-Curie and the Beatriu de Pinós 2021 BP 00168 program. S.M. is funded by Leverhulme Trust grant RPG-2023-240. G.V. and I.S. acknowledge financial support from the SOXS project (PI S. Campana). M.D.S. is funded by the Independent Research Fund Denmark (IRFD, grant 10.46540/2032-00022B) and by an Aarhus University Research Foundation Nova project (AUFF-E-2023-9-28). D.D.S. acknowledges support from the NSFC (grants 12303015 and 12273118), the National Science Foundation of Jiangsu Province (BK20231106), and the China Manned Space Program with grant CMS-CSST- 2025-A20. T.M.R is part of the Cosmic Dawn Center (DAWN), which is funded by the Danish National Research Foundation under grant DNRF140. T.M.R acknowledges support from the Research Council of Finland project 350458. L.G. acknowledges financial support from MCIN and AEI 10.13039/501100011033 under projects PID2023-151307NB-I00, CEX2020-001058-M, and by the MaX-CSIC Excellence Award MaX4-SOMMA-ICE. We thank S. Taubenberger for his observation on 2022-07-01.

We acknowledge the support of the staff of the LJT, XLT, NOT, TNG, GTC, Keck II, KOT, TNT, LT, WMS, and HET. Funding for the LJT has been provided by the CAS and the People's Government of Yunnan Province. The LJT is jointly operated and administrated by YNAO and the Center for Astronomical Mega-Science, CAS. We thank the observers who shared their Keck II NIR observations on WISeREP.

This work is based in part on observations made with the Nordic Optical Telescope, owned in collaboration by the University of Turku and Aarhus University, and operated jointly by Aarhus University, the University of Turku, and the University of Oslo, representing Denmark, Finland, and Norway, the University of Iceland, and Stockholm University, at the Observatorio del Roque de los Muchachos, La Palma, Spain, of the Instituto de Astrofisica de Canarias. Observations from the NOT were obtained through the NUTS2 collaboration, which is supported in part by the Instrument Centre for Danish Astrophysics (IDA), and the Finnish Centre for Astronomy with ESO (FINCA) via Academy of Finland grant 306531. The data presented here were obtained in part with Alhambra Faint Object Spectrograph and Camera (ALFOSC), which is provided by the Instituto de Astrofisica de Andalucia

(IAA) under a joint agreement with the University of Copenhagen and NOTSA. The Liverpool Telescope is operated on the island of La Palma by Liverpool John Moores University in the Spanish Observatorio del Roque de los Muchachos of the Instituto de Astrofisica de Canarias with financial support from the UK Science and Technology Facilities Council. The Italian Telescopio Nazionale Galileo (TNG) operated on the island of La Palma by the Fundación Galileo Galilei of the INAF (Istituto Nazionale di Astrofisica) at the Spanish Observatorio del Roque de los Muchachos of the Instituto de Astrofísica de Canarias. This work is based in part on observations made with the Gran Telescopio Canarias (GTC) under the program GTCMULTIPLE2A-22A, installed at the Spanish Observatorio del Roque de los Muchachos of the Instituto de Astrofísica de Canarias, on the island of La Palma. This article is also based in part on observations made in the Observatorios de Canarias del IAC with the Telescopio Nazionale Galileo, under the program A44TAC_22 (PI G. Valerin).

This work is based in part on observations obtained with the Hobby-Eberly Telescope (HET), which is a joint project of the University of Texas at Austin, the Pennsylvania State University, Ludwig–Maximillians–Universitaet Muenchen, and Georg–August Universitaet Goettingen. The HET is named in honor of its principal benefactors, William P. Hobby and Robert E. Eberly. The Low Resolution Spectrograph 2 (LRS2) was developed and funded by the University of Texas at Austin McDonald Observatory and Department of Astronomy, and by Pennsylvania State University. We thank the Leibniz-Institut fur Astrophysik Potsdam (AIP) and the Institut fur Astrophysik Goettingen (IAG) for their contributions to the construction of the integral field units. We acknowledge the Texas Advanced Computing Center (TACC) at The University of Texas at Austin for providing high-performance computing, visualization, and storage resources that have contributed to the results reported within this paper.

Some of the data presented herein were obtained at the W. M. Keck Observatory, which is operated as a scientific partnership among the California Institute of Technology, the University of California, and NASA; the observatory was made possible by the generous financial support of the W. M. Keck Foundation. A major upgrade of the Kast spectrograph on the Shane 3 m telescope at Lick Observatory, led by Brad Holden, was made possible through generous gifts from the Heising-Simons Foundation, William and Marina Kast, and the University of California Observatories. Research at Lick Observatory is partially supported by a generous gift from Google.

Appendix Supplemental Materials

This appendix compiles supplemental data and methods for SN 2022erq, including the finder chart, observing logs, instrument information, *K*-corrections, and the spectral comparison procedure. Table A1 lists the local reference stars; Table A2 gives the *BVugriz*-band photometry; Table A3 presents the *JHK*-band photometry of SN 2022erq; and Table A4 summarizes the spectroscopic observations. Figure A1 shows a finder chart for SN 2022erq and the local reference stars used in this study. Figure A2 presents the *K*-corrections. Figure A3 displays the GTC and Keck II NIR spectra; the Keck II NIR data are publicly available via WISeREP[33] (O. Yaron & A. Gal-Yam 2012). Figure A4 illustrates the SN-component matching procedure.

Table A1
Local Reference Star on the Field of SN 2022erq

References	*B* (mag)	*V* (mag)	*u* (mag)	*g* (mag)	*r* (mag)	*i* (mag)	*z* (mag)	*J* (mag)	*H* (mag)	*K* (mag)
(1)	15.16(01)	14.60(03)	15.96(01)	14.83(01)	14.52(01)	14.43(01)	14.42(01)	13.58(02)	13.30(02)	13.29(03)
(2)	13.82(03)	13.26(03)	14.86(04)	13.49(01)	13.29(01)	13.13(01)	13.03(01)	12.12(02)	11.87(02)	11.81(02)
(3)	15.92(02)	15.26(03)	16.98(04)	15.53(01)	15.13(01)	15.01(01)	14.99(01)	14.13(03)	13.81(04)	13.78(04)
(4)	15.84(03)	15.10(03)	16.43(20)	16.04(01)	15.03(01)	14.86(01)	14.82(01)	13.78(02)	13.20(03)	13.14(03)
(5)	15.95(03)	15.18(03)	17.08(01)	15.50(01)	14.31(01)	14.19(01)	14.17(01)	13.89(03)	13.48(03)	13.38(04)
(6)	15.02(01)	14.42(03)	15.79(04)	14.66(01)	14.64(01)	14.48(01)	14.42(01)	13.30(02)	12.98(02)	12.94(03)
(7)	15.51(03)	14.78(03)	16.55(02)	15.09(01)	13.21(01)	13.10(01)	13.11(01)	13.47(02)	13.10(03)	13.11(03)
(8)	14.17(03)	13.40(01)	15.23(03)	13.71(01)	12.83(01)	12.53(01)	12.36(01)	12.18(02)	11.88(02)	11.87(02)

Note. Uncertainties are enclosed in parentheses and are 1σ, in units of 0.01 mag.

[33] www.wiserep.org/object/20439

Table A2
BVugriz − band Photometry of SN 2022erq

MJD	τ[a] (days)	t[b] (days)	*B* (mag)	*V* (mag)	*u* (mag)	*g* (mag)	*r* (mag)	*i* (mag)	*z* (mag)	Telescope
59650.93	1.83	−23.77	⋯	⋯	17.87(09)	17.75(01)	17.60(02)	17.96(02)	17.39(06)	LJT
59651.94	2.84	−22.76	⋯	⋯	⋯	17.50(02)	17.40(02)	17.65(03)	⋯	WMS
59652.88	3.78	−21.82	⋯	⋯	17.43(12)	17.29(03)	17.26(03)	17.48(03)	17.25(05)	WMS
59654.17	5.07	−20.53	17.34(07)	16.88(20)	17.14(08)	⋯	⋯	⋯	⋯	ST
59654.93	5.83	−19.77	⋯	⋯	⋯	17.04(02)	16.99(02)	17.26(03)	⋯	WMS
59655.92	6.82	−18.78	⋯	⋯	17.04(05)	16.88(03)	17.02(03)	17.14(03)	17.07(06)	LJT
59655.95	6.85	−18.75	⋯	⋯	⋯	16.85(04)	16.94(04)	17.06(08)	⋯	WMS
59656.93	7.83	−17.77	⋯	⋯	⋯	16.80(03)	16.88(02)	17.02(02)	⋯	LJT
59656.93	7.83	−17.77	⋯	⋯	⋯	16.81(02)	16.82(02)	16.99(02)	⋯	WMS
59657.91	8.81	−16.79	⋯	⋯	⋯	16.78(01)	16.78(02)	16.93(03)	⋯	WMS
59658.84	9.74	−15.86	16.96(03)	16.73(03)	⋯	16.74(01)	16.76(03)	16.95(04)	⋯	TNT
59658.84	9.74	−15.86	⋯	⋯	⋯	16.69(03)	16.70(02)	16.85(03)	⋯	WMS
59659.86	10.76	−14.84	16.88(03)	16.65(03)	⋯	16.72(01)	16.67(03)	16.87(03)	⋯	TNT
59659.87	10.77	−14.83	⋯	⋯	⋯	16.61(04)	16.62(03)	16.82(02)	⋯	LJT
59659.90	10.80	−14.80	⋯	⋯	⋯	16.60(02)	16.64(02)	16.72(02)	⋯	WMS
59660.84	11.74	−13.86	⋯	⋯	⋯	16.47(02)	16.60(02)	16.71(02)	⋯	WMS
59661.10	12.00	−13.60	16.73(02)	16.53(01)	16.91(07)	16.57(01)	16.60(01)	16.64(01)	⋯	ST
59661.89	12.79	−12.81	⋯	⋯	⋯	16.39(04)	16.55(04)	16.64(06)	⋯	WMS
59662.84	13.74	−11.86	⋯	⋯	⋯	16.39(01)	16.48(02)	16.58(02)	⋯	WMS
59663.16	14.06	−11.54	16.69(03)	⋯	16.85(07)	16.53(01)	16.52(01)	⋯	16.74(02)	LT
59663.83	14.73	−10.87	⋯	⋯	⋯	16.51(04)	16.45(04)	16.55(06)	⋯	WMS
59664.16	15.06	−10.54	⋯	16.44(02)	16.79(05)	16.54(03)	16.50(02)	⋯	16.68(02)	LT
59665.88	16.78	−8.82	⋯	⋯	⋯	16.34(01)	16.41(02)	16.48(02)	⋯	WMS
59665.89	16.79	−8.81	16.69(06)	16.43(05)	⋯	⋯	⋯	⋯	⋯	TNT
59667.88	18.78	−6.82	⋯	⋯	16.79(09)	16.32(01)	16.37(01)	16.40(02)	⋯	WMS
59668.17	19.07	−6.53	16.61(02)	16.31(02)	16.83(06)	16.43(01)	16.37(01)	⋯	⋯	LT
59668.86	19.76	−5.84	⋯	⋯	⋯	16.32(01)	16.34(01)	16.37(02)	⋯	WMS
59669.17	20.07	−5.53	⋯	16.33(02)	16.92(05)	16.43(01)	16.36(01)	16.43(01)	16.59(02)	LT
59672.86	23.76	−1.84	16.59(03)	16.30(03)	⋯	16.43(01)	16.28(03)	16.38(02)	⋯	TNT
59675.78	26.68	1.08	16.57(03)	16.31(02)	⋯	16.45(02)	16.27(03)	16.35(03)	⋯	TNT
59677.06	27.96	2.36	⋯	⋯	17.04(06)	16.37(01)	16.20(01)	16.24(01)	⋯	ST
59678.90	29.80	4.20	⋯	⋯	17.08(05)	16.30(01)	16.10(01)	16.24(01)	⋯	LJT
59680.06	30.96	5.36	⋯	⋯	17.08(07)	16.34(01)	16.17(01)	16.20(01)	⋯	ST
59681.20	32.10	6.50	⋯	⋯	⋯	⋯	⋯	⋯	16.39(01)	LT
59683.08	33.98	8.38	⋯	⋯	⋯	16.32(01)	16.17(01)	16.19(01)	⋯	ST
59683.10	34.00	8.40	⋯	⋯	17.18(05)	⋯	⋯	⋯	16.37(01)	LT
59684.80	35.70	10.10	⋯	⋯	17.26(05)	16.36(01)	⋯	16.23(02)	⋯	LJT
59685.79	36.69	11.09	16.69(03)	16.27(03)	⋯	16.47(01)	⋯	⋯	⋯	TNT
59687.06	37.96	12.36	⋯	⋯	⋯	16.43(01)	16.22(01)	16.15(01)	⋯	ST
59687.79	38.69	13.09	16.77(04)	16.31(03)	⋯	16.52(04)	16.22(05)	16.31(03)	⋯	TNT
59688.85	39.75	14.15	16.82(02)	16.35(03)	⋯	16.51(01)	16.22(03)	16.30(03)	⋯	TNT
59691.13	42.03	16.43	16.77(04)	16.32(02)	17.42(08)	16.52(02)	16.24(01)	16.22(01)	16.42(01)	LT
59691.77	42.67	17.07	⋯	⋯	⋯	16.53(02)	16.29(02)	16.25(01)	⋯	LJT
59691.80	42.70	17.10	16.90(03)	16.37(02)	⋯	16.58(02)	16.24(03)	16.30(03)	⋯	TNT
59692.80	43.70	18.10	16.94(03)	16.40(03)	⋯	16.63(01)	16.28(03)	16.30(03)	⋯	TNT
59692.88	43.78	18.18	⋯	⋯	⋯	16.54(02)	16.37(01)	16.14(03)	⋯	LJT
59693.10	44.00	18.40	16.86(03)	⋯	17.46(08)	16.62(02)	16.25(01)	16.22(01)	16.37(01)	LT
59696.73	47.63	22.03	16.97(04)	16.43(03)	⋯	16.64(02)	16.31(01)	16.25(02)	⋯	LJT
59697.08	47.98	22.38	⋯	⋯	⋯	⋯	⋯	⋯	16.44(02)	LT
59697.09	47.99	22.39	⋯	⋯	⋯	16.68(01)	16.29(01)	16.25(01)	⋯	ST
59699.79	50.69	25.09	17.20(03)	16.54(03)	⋯	16.80(01)	16.37(03)	16.39(03)	⋯	TNT
59700.80	51.70	26.10	17.27(06)	16.56(03)	⋯	16.83(02)	16.37(03)	16.39(03)	⋯	TNT
59701.16	52.06	26.46	17.13(03)	16.53(02)	17.77(06)	16.80(01)	16.38(01)	16.31(01)	16.49(02)	LT
59701.78	52.68	27.08	17.31(05)	16.55(03)	⋯	16.85(02)	16.37(03)	16.34(03)	⋯	TNT
59702.78	53.68	28.08	17.24(04)	16.55(03)	⋯	16.86(02)	16.37(03)	⋯	⋯	TNT
59705.12	56.02	30.42	17.28(02)	16.63(02)	17.78(04)	16.93(01)	16.44(01)	16.37(01)	16.50(01)	LT
59706.77	57.67	32.07	17.36(07)	16.66(05)	17.97(09)	16.97(02)	16.48(01)	16.36(07)	⋯	LJT
59709.05	59.95	34.35	⋯	⋯	⋯	⋯	⋯	⋯	16.50(03)	LT
59710.06	60.96	35.36	⋯	⋯	⋯	17.10(01)	16.49(01)	16.39(01)	⋯	ST
59710.99	61.89	36.29	⋯	16.77(02)	⋯	⋯	⋯	⋯	⋯	ST
59714.76	65.66	40.06	17.70(03)	16.88(03)	⋯	17.24(02)	16.54(04)	16.55(03)	⋯	TNT
59716.06	66.96	41.36	⋯	⋯	⋯	⋯	⋯	⋯	16.62(01)	LT
59716.76	67.66	42.06	17.72(03)	16.89(03)	⋯	17.36(03)	16.60(03)	16.61(03)	⋯	TNT

Table A2
(Continued)

MJD	τ[a] (days)	t[b] (days)	B (mag)	V (mag)	u (mag)	g (mag)	r (mag)	i (mag)	z (mag)	Telescope
59719.06	69.96	44.36	17.78(02)	16.94(02)	⋯	17.27(01)	16.67(01)	16.49(01)	⋯	ST
59719.79	70.69	45.09	17.82(02)	17.01(02)	⋯	17.41(01)	16.71(03)	16.67(02)	⋯	TNT
59720.70	71.60	46.00	17.87(04)	16.99(03)	⋯	17.36(02)	16.68(03)	16.69(03)	⋯	TNT
59721.68	72.58	46.98	17.97(03)	17.03(02)	⋯	17.38(03)	16.75(04)	16.63(03)	⋯	TNT
59722.68	73.58	47.98	17.88(03)	17.05(02)	⋯	17.40(02)	16.73(03)	16.72(03)	⋯	TNT
59725.62	76.52	50.92	18.04(03)	17.10(03)	⋯	17.50(02)	16.78(03)	16.70(03)	⋯	TNT
59727.05	77.95	52.35	18.04(02)	17.09(01)	⋯	17.49(01)	16.82(01)	16.63(01)	⋯	ST
59727.71	78.61	53.01	18.04(03)	17.13(02)	⋯	17.56(02)	16.87(03)	16.69(03)	⋯	TNT
59728.73	79.63	54.03	18.03(03)	17.16(02)	⋯	17.59(02)	16.84(03)	16.83(03)	⋯	TNT
59729.16	80.06	54.46	⋯	⋯	⋯	⋯	⋯	⋯	16.81(01)	LT
59730.75	81.65	56.05	18.12(04)	17.22(02)	⋯	17.59(02)	16.88(03)	16.85(03)	⋯	TNT
59731.97	82.87	57.27	⋯	⋯	⋯	⋯	⋯	⋯	16.80(02)	LT
59732.76	83.66	58.06	18.02(03)	17.22(02)	⋯	17.62(02)	16.95(02)	16.83(02)	⋯	LJT
59735.05	85.95	60.35	⋯	⋯	⋯	17.67(01)	16.95(01)	16.77(02)	⋯	ST
59736.64	87.54	61.94	18.29(05)	17.33(04)	⋯	17.72(03)	17.04(04)	16.95(03)	⋯	TNT
59742.07	92.97	67.37	⋯	⋯	⋯	17.72(01)	17.12(01)	⋯	⋯	ST
59743.03	93.93	68.33	18.32(03)	17.33(02)	⋯	⋯	⋯	16.89(01)	⋯	ST
59744.94	95.84	70.24	⋯	⋯	⋯	⋯	⋯	⋯	16.95(03)	LT
59748.73	99.63	74.03	18.28(03)	17.37(02)	⋯	17.77(02)	17.20(02)	17.07(01)	⋯	LJT
59754.99	105.89	80.29	18.36(02)	17.48(01)	⋯	17.89(01)	17.28(01)	17.11(01)	⋯	ST
59768.01	118.91	93.31	⋯	⋯	⋯	⋯	⋯	⋯	17.24(02)	LT
59768.96	119.86	94.26	18.59(02)	17.71(02)	⋯	17.98(01)	17.51(01)	17.33(01)	⋯	ST
59772.98	123.88	98.28	18.88(23)	17.87(17)	⋯	18.01(16)	17.50(14)	17.42(14)	17.38(29)	KOT
59775.99	126.89	101.29	18.82(21)	17.86(15)	⋯	18.07(16)	17.49(14)	17.36(13)	17.32(17)	KOT
59778.95	129.85	104.25	18.63(16)	17.84(12)	⋯	18.18(12)	17.60(10)	17.44(10)	17.42(12)	KOT
59781.94	132.84	107.24	18.99(17)	17.92(09)	⋯	18.23(11)	17.66(07)	17.57(06)	17.64(10)	KOT
59784.93	135.83	110.23	18.97(19)	17.95(10)	⋯	18.26(13)	17.63(09)	17.61(07)	17.41(11)	KOT
59786.96	137.86	112.26	⋯	⋯	⋯	⋯	⋯	⋯	17.57(03)	LT
59788.92	139.82	114.22	18.91(18)	18.01(10)	⋯	18.32(12)	17.72(08)	17.62(06)	17.47(11)	KOT
59792.91	143.81	118.21	18.94(17)	18.10(10)	⋯	18.43(11)	17.79(08)	17.64(06)	17.66(12)	KOT
59794.02	144.92	119.32	⋯	17.97(02)	⋯	18.32(01)	17.77(01)	17.61(01)	⋯	ST
59795.90	146.80	121.20	19.05(17)	18.06(08)	⋯	18.40(10)	17.82(07)	17.64(06)	17.61(12)	KOT
59797.88	148.78	123.18	⋯	⋯	⋯	⋯	⋯	⋯	17.65(02)	LT
59798.89	149.79	124.19	⋯	⋯	⋯	⋯	⋯	⋯	17.71(03)	LT
59798.92	149.82	124.22	19.05(27)	18.08(13)	⋯	18.58(15)	17.81(09)	17.74(08)	17.75(16)	KOT
59801.88	152.78	127.18	18.94(21)	18.04(11)	⋯	18.47(14)	18.00(08)	17.75(06)	17.70(15)	KOT
59805.87	156.77	131.17	19.19(45)	18.26(15)	⋯	18.62(15)	18.04(12)	17.85(11)	17.80(16)	KOT
59808.89	159.79	134.19	19.24(21)	18.25(13)	⋯	18.49(13)	17.99(11)	17.81(10)	17.93(18)	KOT
59816.86	167.76	142.16	⋯	⋯	⋯	⋯	⋯	⋯	17.90(02)	LT
59816.88	167.78	142.18	19.24(20)	18.46(12)	⋯	18.67(11)	18.17(10)	18.02(10)	17.97(17)	KOT
59817.53	168.43	142.83	19.09(05)	18.25(04)	⋯	18.69(03)	18.03(03)	18.09(04)	⋯	TNT
59822.57	173.47	147.87	19.19(05)	18.30(04)	⋯	18.66(03)	18.04(03)	18.11(04)	⋯	TNT
59823.54	174.44	148.84	19.10(06)	18.33(04)	⋯	18.69(02)	18.08(04)	18.12(03)	⋯	TNT
59823.87	174.77	149.17	19.25(22)	18.46(16)	⋯	18.71(17)	18.34(18)	17.88(15)	17.82(24)	KOT
59824.69	175.59	149.99	19.21(10)	18.44(06)	⋯	⋯	⋯	⋯	⋯	TNT
59825.98	176.88	151.28	⋯	⋯	⋯	⋯	⋯	⋯	17.92(03)	LT
59827.00	177.90	152.30	⋯	18.44(03)	⋯	18.68(02)	18.29(02)	18.11(02)	⋯	ST
59827.60	178.50	152.90	19.06(04)	18.37(04)	⋯	18.79(05)	18.17(03)	18.23(03)	⋯	TNT
59828.59	179.49	153.89	19.11(06)	18.36(04)	⋯	18.77(04)	18.11(03)	18.19(04)	⋯	TNT
59829.60	180.50	154.90	19.21(07)	18.41(04)	⋯	18.79(06)	18.29(04)	18.24(04)	⋯	TNT
59834.90	185.80	160.20	19.33(59)	18.51(19)	⋯	18.76(17)	18.46(13)	18.06(13)	18.01(34)	KOT
59838.85	189.75	164.15	⋯	⋯	⋯	⋯	⋯	⋯	18.10(05)	LT
59839.93	190.83	165.23	19.52(04)	18.53(02)	⋯	18.82(02)	18.49(02)	18.12(02)	⋯	ST
59840.60	191.50	165.90	19.28(05)	18.43(04)	⋯	18.80(03)	18.25(03)	18.25(04)	⋯	TNT
59845.79	196.69	171.09	19.54(20)	18.77(15)	⋯	19.02(15)	18.48(13)	18.24(13)	18.25(22)	KOT
59853.51	204.41	178.81	19.49(06)	18.69(03)	⋯	19.02(03)	18.60(03)	18.34(03)	⋯	LJT
59856.59	207.49	181.89	19.33(09)	18.62(07)	⋯	18.97(05)	18.33(04)	18.20(07)	⋯	TNT
59856.93	207.83	182.23	19.74(33)	18.91(18)	⋯	19.16(17)	18.49(12)	18.53(14)	⋯	KOT
59858.57	209.47	183.87	19.41(10)	18.64(05)	⋯	18.94(07)	18.45(04)	18.40(05)	⋯	TNT
59859.85	210.75	185.15	19.48(11)	18.78(05)	⋯	⋯	18.64(04)	18.49(03)	18.24(04)	LT
59861.53	212.43	186.83	19.51(15)	18.88(12)	⋯	19.03(12)	18.43(06)	18.41(05)	⋯	TNT
59862.58	213.48	187.88	19.59(19)	18.73(10)	⋯	19.07(12)	18.42(06)	⋯	⋯	TNT
59868.89	219.79	194.19	19.70(34)	18.96(19)	⋯	19.11(21)	18.59(13)	18.63(16)	18.42(14)	KOT

Table A2
(Continued)

MJD	τ[a] (days)	t[b] (days)	B (mag)	V (mag)	u (mag)	g (mag)	r (mag)	i (mag)	z (mag)	Telescope
59869.91	220.81	195.21	19.70(06)	18.82(04)	⋯	19.09(03)	18.69(03)	⋯	18.26(05)	LT
59872.56	223.46	197.86	19.66(09)	18.75(04)	⋯	19.12(04)	18.51(03)	18.49(05)	⋯	LJT
59873.50	224.40	198.80	⋯	18.81(02)	⋯	⋯	18.75(02)	18.61(03)	18.26(04)	LJT
59879.49	230.39	204.79	19.79(06)	18.86(03)	⋯	19.15(03)	18.89(02)	18.63(03)	⋯	LJT
59879.85	230.75	205.15	19.91(23)	18.99(15)	⋯	19.15(13)	18.69(10)	18.48(10)	18.45(24)	KOT
59885.50	236.40	210.80	⋯	18.89(03)	⋯	⋯	18.83(03)	18.72(03)	18.34(04)	LJT
59893.49	244.39	218.79	19.89(09)	19.03(03)	⋯	19.33(04)	18.93(03)	18.77(03)	18.39(05)	LJT
59896.48	247.38	221.78	20.20(10)	19.01(05)	⋯	19.24(03)	19.01(03)	18.83(04)	18.45(04)	LJT
59896.69	247.59	221.99	19.87(23)	19.02(18)	⋯	19.30(17)	18.80(13)	18.46(13)	18.43(21)	KOT
59898.49	249.39	223.79	20.01(05)	18.99(04)	⋯	19.27(02)	18.93(03)	18.76(03)	⋯	LJT
59898.86	249.76	224.16	19.69(09)	19.11(06)	⋯	19.52(06)	19.15(06)	18.82(03)	⋯	LT
59903.50	254.40	228.80	20.05(06)	19.14(04)	⋯	19.45(04)	19.18(04)	18.81(03)	18.53(05)	LJT
59913.48	264.38	238.78	⋯	19.17(06)	⋯	⋯	19.06(05)	18.73(04)	⋯	LJT
59920.48	271.38	245.78	⋯	⋯	⋯	⋯	19.35(12)	19.00(10)	⋯	LJT
59941.19	292.09	266.49	20.18(48)	19.36(39)	⋯	19.61(33)	19.15(20)	19.07(26)	⋯	KOT
59969.16	320.06	294.46	20.40(28)	19.38(20)	⋯	19.83(19)	19.31(14)	19.23(12)	19.24(23)	KOT
59981.09	331.99	306.39	⋯	⋯	⋯	⋯	⋯	19.46(26)	19.43(46)	KOT
59986.08	336.98	311.38	⋯	19.68(38)	⋯	19.93(30)	19.44(20)	19.43(24)	19.40(23)	KOT
59991.05	341.95	316.35	⋯	⋯	⋯	19.92(33)	19.52(21)	19.48(20)	19.46(26)	KOT
59992.94	343.84	318.24	⋯	⋯	⋯	⋯	19.68(05)	19.52(03)	⋯	LJT
59993.91	344.81	319.21	⋯	⋯	⋯	19.99(14)	⋯	⋯	⋯	LJT
60005.05	355.95	330.35	20.82(48)	⋯	⋯	20.29(50)	19.89(32)	19.59(30)	19.57(13)	KOT
60013.07	363.97	338.37	⋯	20.34(13)	⋯	⋯	20.09(46)	19.63(41)	⋯	KOT
60019.97	370.87	345.27	⋯	⋯	⋯	⋯	20.59(29)	20.19(40)	⋯	KOT
60024.98	375.88	350.28	21.56(35)	20.78(41)	⋯	21.03(38)	20.63(21)	20.23(17)	⋯	KOT
60032.01	382.91	357.31	21.75(53)	⋯	⋯	⋯	20.82(73)	20.41(45)	⋯	KOT
60049.86	400.76	375.16	⋯	⋯	⋯	⋯	20.69(10)	20.47(39)	20.12(19)	LJT
60052.90	403.80	378.20	⋯	⋯	⋯	⋯	20.93(16)	20.61(11)	⋯	LJT
60087.84	438.74	413.14	22.53(30)	21.65(26)	⋯	22.03(20)	21.62(25)	21.37(23)	⋯	LJT
60091.88	442.78	417.18	⋯	⋯	⋯	22.16(15)	21.66(25)	21.47(36)	⋯	LJT
60092.88	443.78	418.18	⋯	⋯	⋯	⋯	22.43(30)	22.05(49)	⋯	LJT
60125.60	476.50	450.90	⋯	⋯	⋯	⋯	23.15(43)	⋯	⋯	LJT

Notes. Uncertainties are enclosed in parentheses and are 1σ, in units of 0.01 mag.
[a] The phase relative to the day of explosion, MJD = 59649.1.
[b] The phase relative to the day of *B*-band maximum, MJD = 59674.7.

Table A3
JHK − band Photometry of SN 2022erq Obtained by NOTCam of NOT

MJD	τ[a] (days)	t[b] (days)	J (mag)	H (mag)	K (mag)
59683.70	34.60	9.00	15.73(01)	15.52(01)	15.51(02)
59809.70	160.60	135.00	17.34(01)	16.97(04)	16.88(02)
59837.64	188.54	162.94	17.64(03)	17.35(03)	17.21(03)
59882.47	233.37	207.77	17.92(04)	17.59(03)	17.49(04)
59997.86	348.76	323.16	18.21(09)	18.05(05)	17.49(08)
60018.77	369.67	344.07	18.68(08)	18.18(07)	17.58(05)
60060.71	411.61	386.01	18.94(05)	18.32(08)	17.67(07)

Notes. Uncertainties are enclosed in parentheses and are 1σ, in units of 0.01 mag.
[a] The phase relative to the day of explosion, MJD = 59649.1.
[b] The phase relative to the day of *B*-band maximum, MJD = 59674.7.

A.1. Facilities

Photometric observations were obtained by the Li–Jiang 2.4 m telescope (LJT; Y.-F. Fan et al. 2015) and the Wumingshan 60 cm Telescope (WMS) of Yunnan Observatories, the Konkoly Observatory 0.8 m RC 80 robotic telescope (KOT), the Tsinghua-NAOC 0.8 m Telescope (TNT) at Xinglong Observatory, the Liverpool 2.0 m Telescope (LT), and the 67/91 cm Schmidt Telescope (ST). They were observed in the *JHK* band by the 2.56 m Nordic Optical Telescope (NOT) at Roque de los Muchachos Observatory also.

Spectroscopic observations were carried out using various facilities, as follows:

1. Yunnan Faint Object Spectrograph and Camera (YFOSC; C.-J. Wang et al. 2019) on the LJT;
2. Beijing Faint Object Spectrograph and Camera (BFOSC) on the Xinglong 2.16 m telescope (XLT) at the National Astronomical Observatories (J.-C. Zhang et al. 2016); due to operational constraints, the slit could not be oriented at the parallactic angle;
3. Kast Double Spectrograph (KDS) on the 3 m Shane telescope at Lick Observatory (J. Miller & R. Stone 1994);
4. ALFOSC on the NOT;
5. Device Optimized for Low Resolution (DOLORES) with various grisms (low-resolution LRB/LRR and higher-

Table A4
Journal of Spectroscopic Observations of SN 2022erq

Date (YYMMDD)	MJD	Epoch[a] (days)	Range (Å)	R [b]	Telescope+Inst.
220312	59650.902	1.8	3488–8742	360	LJT+YFOSC
220315	59653.904	4.8	3498–8767	320	LJT+YFOSC
220320	59658.850	9.7	3875–8854	300	XLT+BFOSC
220321	59659.843	11	3486–8742	420	LJT+YFOSC
220324	59662.517	13	3620–10670	470	Shane+KDS
220330	59668.219	19	3425–9701	430	NOT+ALFOSC
220330	59668.239	19	6134–7772	1420	TNG+VHR
220409	59678.873	30	3486–8742	400	LJT+YFOSC
220411	59680.182	31	3410–9665	350	NOT+ALFOSC
220415	59684.777	36	3503–8768	300	LJT+YFOSC
220421	59691.147	42	3500–10318	570	TNG+LRB/LRR
220424	59693.850	45	3497–8484	300	LJT+YFOSC
220512	59711.686	63	3862–8831	370	XLT+BFOSC
220512	59711.709	63	3474–8766	320	LJT+YFOSC
220513	59712.723	64	3862–8831	380	XLT+BFOSC
220520	59719.746	71	3874–8839	410	XLT+BFOSC
220526	59726.148	77	6139–7774	1420	TNG+VHR
220618	59748.085	99	3422–10071	410	NOT+ALFOSC
220712	59772.122	123	3424–9700	450	NOT+ALFOSC
220805	59796.399	147	3623–8107	1620	Shane+KDS
220808	59799.064	150	8960–13296	…	GTC+EMIR
220826	59817.614	169	3897–8876	370	XLT+BFOSC
220917	59839.468	190	3891–8869	380	XLT+BFOSC
220925	59847.189	198	3622–9998	550	Shane+KDS
221018	59870.594	221	3896–8868	360	XLT+BFOSC
221027	59879.524	230	3520–8784	350	LJT+YFOSC
221109	59892.489	243	3521–8783	400	LJT+YFOSC
230301	60004.890	356	3631–8947	300	LJT+YFOSC
230316	60019.539	370	3622–10000	500	Shane+KDS
230322	60025.619	377	4500–9650	1550	KeckII+DEIMOS
230709	60137.280	488	3650–10000	1800	HET+LRS2
251108	60987.490	1338	3850–7420	630	LJT+YFOSC
251116	60995.480	1346	3643–8863	350	LJT+YFOSC

Notes. LRB is low-resolution grism; LRR is low-resolution red grism; VHR is very high resolution grism.
[a] The epoch is relative to the derived explosion date, MJD = 59649.1.
[b] The spectral resolving power $R = \lambda/\Delta\lambda$, where $\lambda = 6300$ Å; $\Delta\lambda$ is derived by the FWHM of the night-sky line [O I] λ6300.3, except for the NIR spectrum from GTC.

resolution VHR) on the 3.58 m Telescopio Nazionale Galileo (TNG) at Roque de los Muchachos Observatory;
6. Espectrógrafo Multiobjeto Infrarrojo (EMIR) on the 10.4 m Gran Telescopio Canarias (GTC) at Roque de los Muchachos Observatory;
7. Deep Extragalactic Imaging Multi-Object Spectrograph (DEIMOS) and Near Infrared Echellette Spectrograph (NIRES) on the 10 m Keck II telescope at W. M. Keck Observatory;
8. Low Resolution Spectrograph-2 (LRS2; H. Lee et al. 2010) on the 9.2 m Hobby-Eberly Telescope (HET) at McDonald Observatory.

LRS2 is an integral field spectrograph equipped with lenslets and a fiber array (commonly referred to as an integral field unit, or IFU). Given that the host galaxy of SN 2022erq has an optical extent of $\sim 5'' \times 6''$ and the SN is located at a projected angular distance of $\sim 1\overset{''}{.}5$ from the galactic center, the IFU's field of view of $7'' \times 12''$ (with a fill factor close to 100%) readily encompasses the entire galaxy and the SN position. The spectral features extracted specifically from the location of SN 2022erq are consistent with the spectrum from other regions of the galaxy. This indicates that, at the epoch of observation, the contribution from the SN itself is minimal, and the obtained spectrum is dominated by the integrated light of the host galaxy. Therefore, as an IFU-based spectrograph, LRS2 is an ideal facility for studying the environment of the SN.

The DEIMOS detector has a CCD array in which all spectra cross a small chip gap. In the case of SN 2022erq, this chip gap is located right at the position of Hα emission (from ∼6548 to 6560 Å in the rest frame). This resulted in the loss of a segment of the narrow Hα flux, as part of the line profile fell within the gap. For this reason, the narrow Hα component from this spectrum ($\tau \approx 377$ days) was not used for flux measurements and quantitative analysis.

A.2. Methodology for Spectral Comparison

We employed a custom spectral-matching algorithm to compare the spectra of SN 2022erq with those of well-observed SN Ia templates (M. Hamuy et al. 2003; G. Aldering et al. 2006). The procedure automatically processes pairs of spectra over a wide range of postexplosion phases and

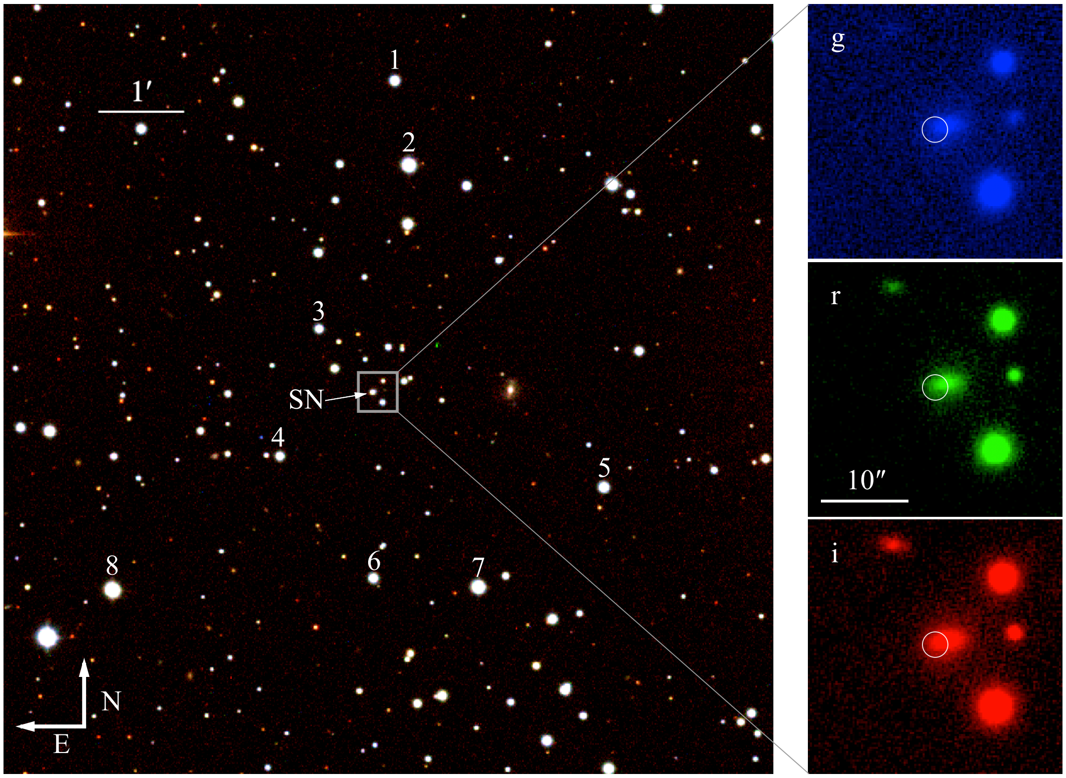

Figure A1. Composite *gri*-band finder chart of SN 2022erq and local reference stars obtained on 2022 June (left), alongside a preexplosion Pan-STARRS *gri*-band image (right). The position of SN is indicated by a white circle (radius = 1″5), matching the typical image FWHM.

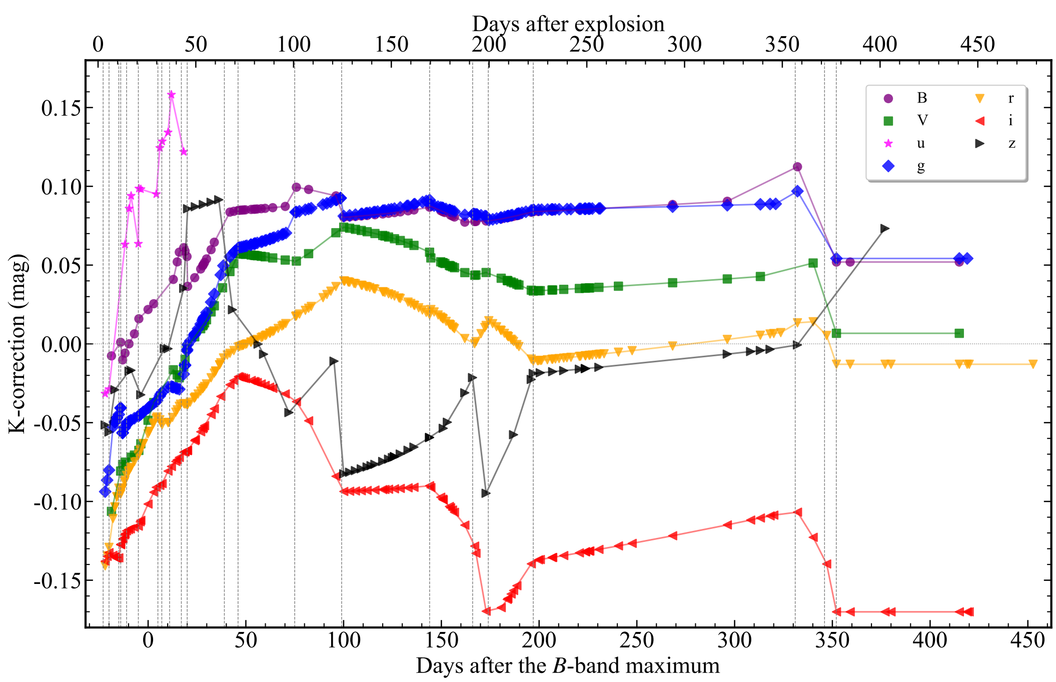

Figure A2. K-correction for the *BVugriz* − band light curves of SN 2022erq, derived from spectra obtained at comparable phases. Epochs with spectroscopic observations are indicated by vertical dashed lines.

identifies spectrally similar matches. To allow for the slower spectral evolution expected in strongly interacting events, we do not restrict ourselves to strictly contemporaneous phases, but instead permit phase differences of up to 120 days.

Each spectrum is first corrected for redshift and scaled to a common flux normalization by multiplying by $4\pi D^2$, where D is the distance. The core of the matching process involves computing an initial difference between the SN 2022erq spectrum and a given template, and fitting this difference with a third-order polynomial as a smooth, wavelength-dependent correction to the continuum. Adding this polynomial to the template spectrum yields a "matched" spectrum for direct comparison with SN 2022erq.

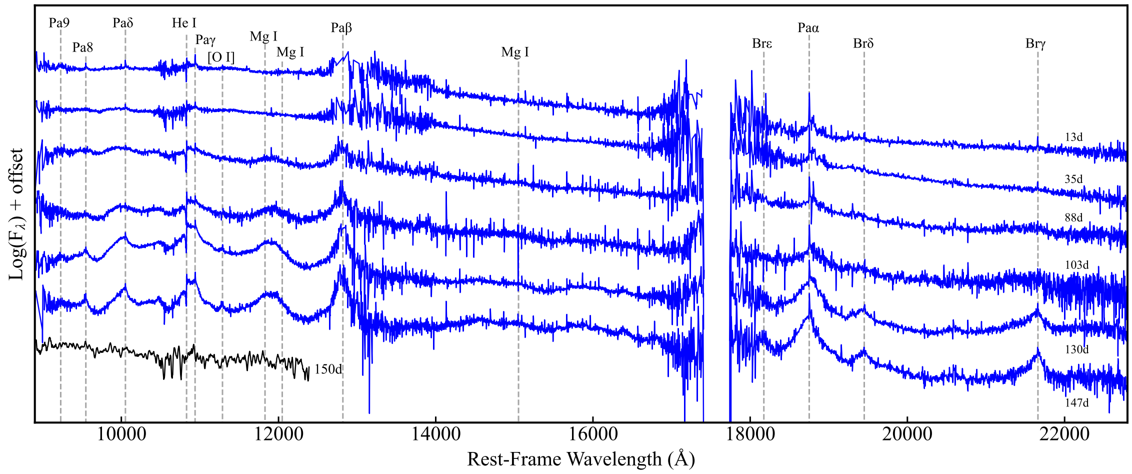

Figure A3. NIR spectra of SN 2022erq obtained by EMIR at GTC (black) and NIRES at Keck II (blue). The public spectra of Keck are available through WISeREP. The dashed lines mark the narrow emission features at the rest wavelength. The phases of each spectrum are relative to the explosion date (MJD = 59649.1). (See Figure 2 for data availability.)

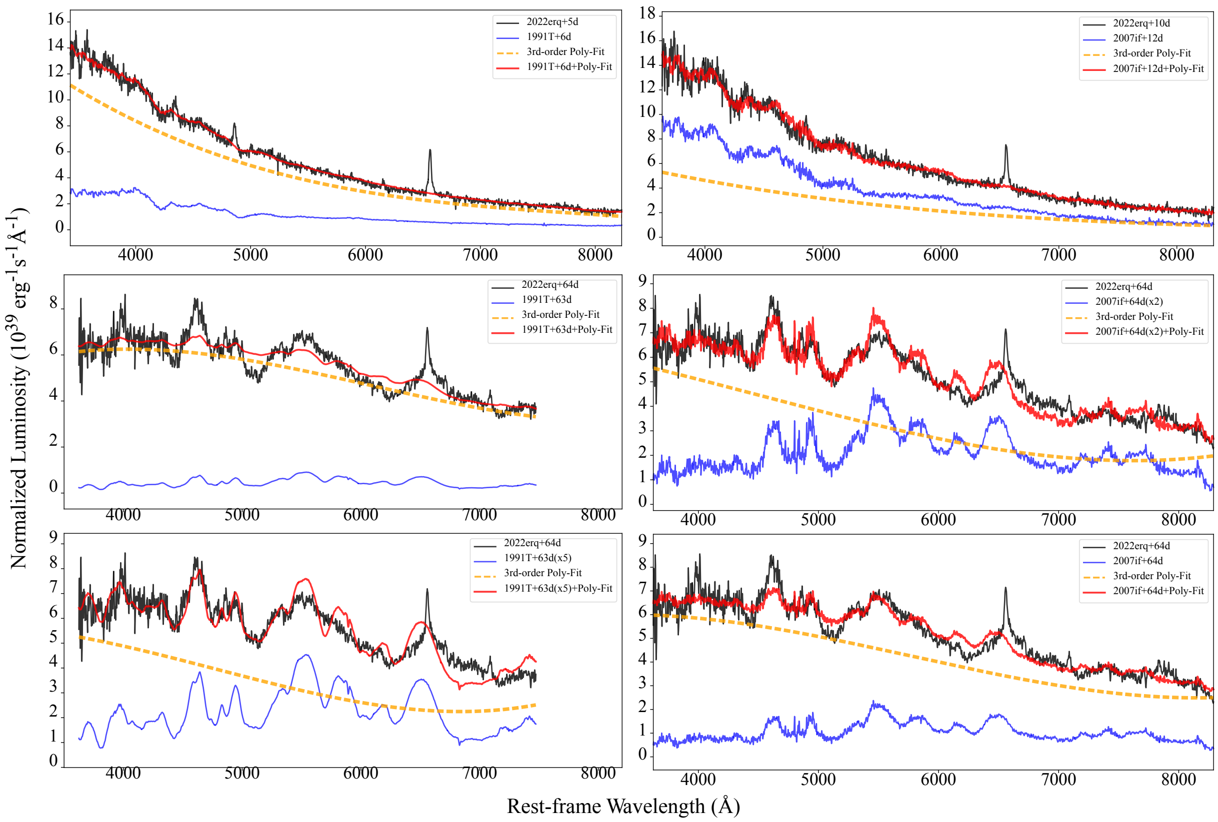

Figure A4. An illustration of the spectral matching procedure. The spectra of the comparison SNe were corrected for redshift and distance, and then combined with a third-order polynomial fit to match the corresponding continuum of SN 2022erq. For phases where the template luminosity differs significantly from that of SN 2022erq, such as $\tau > 60$ days in the case of SNe 1991T ($\times 5$) and 2007if ($\times 2$), an additional flux scaling is applied prior to polynomial fitting to preserve the strength of spectral features.

In cases where the luminosities of the template and SN 2022erq differ substantially, a polynomial continuum correction alone can dilute the spectral features of the matched template. To mitigate this, we first apply a global flux scaling to the template prior to the polynomial fitting. The scaling factor is chosen such that the flux level around relatively isolated Fe II $\lambda\lambda$4549, 4629 features approximately matches that of SN 2022erq. The third-order polynomial is then fitted to the residual difference after this scaling, and the sum of the scaled template and polynomial correction is taken as the final matched spectrum. As illustrated in Figure A4, this step is particularly important at $\tau \gtrsim 60$ days, where the luminosities of SN 1991T and SN 2007if are much lower than that of SN 2022erq.

The quality of each match is quantified by a set of residual-based metrics. Let $F_{\rm SN}(\lambda)$ be the flux of SN 2022erq and $F_{\rm temp,fit}(\lambda)$ be the matched template (i.e., template plus polynomial correction). We define the absolute residual

$$R(\lambda) = F_{\rm SN}(\lambda) - F_{\rm temp,fit}(\lambda),$$

and the relative residual

$$R_{\rm rel}(\lambda) = \frac{R(\lambda)}{|F_{\rm SN}(\lambda)| + \epsilon},$$

where the small constant ϵ prevents division by zero. Over wavelength regions that exclude strong CSM emission lines and areas of severe blending, we compute for both R and $R_{\rm rel}$ the mean, standard deviation, and rms. We also record the minimum, maximum, and range of R, as well as higher-order statistics such as the skewness and kurtosis of the residual distribution. Additional rms quantities are computed for (i) the difference between $F_{\rm SN}$ and the uncorrected template plus polynomial fit and (ii) the difference between the original template and the SN spectrum with the polynomial term subtracted, to assess the internal consistency of the continuum correction.

Among all candidate template spectra for a given SN 2022erq epoch, we use the rms of the relative residual, rms($R_{\rm rel}$), as our primary ranking statistic, and identify the three templates with the smallest values as the best matches. For these top-ranked matches, we further examine the absolute rms residuals and phase differences and visually inspect the spectra to ensure that the selected matches are morphologically plausible.

We emphasize that, because the spectra of SN 2022erq are strongly affected by CSM interaction (continuum boosting and line dilution), even small differences in rms residuals do not uniquely determine the intrinsic SN Ia subtype. The spectral comparisons are therefore used in a heuristic sense: to demonstrate that SN 2022erq shares an efficient-burning spectroscopic phenotype (iron-group dominance and weak IMEs) with both 91T-like and some SC SNe Ia, rather than to identify a single, uniquely "best" template.

ORCID iDs

Qian Zhai https://orcid.org/0009-0002-3956-6143
Jujia Zhang https://orcid.org/0000-0002-8296-2590
Xiaofeng Wang https://orcid.org/0000-0002-7334-2357
A. Pastorello https://orcid.org/0000-0002-7259-4624
Alexei V. Filippenko https://orcid.org/0000-0003-3460-0103
József Vinkó https://orcid.org/0000-0001-8764-7832
Thomas G. Brink https://orcid.org/0000-0001-5955-2502
Yunkun Han https://orcid.org/0000-0002-2547-0434
G. Valerin https://orcid.org/0000-0002-3334-4585
N. Elias Rosa https://orcid.org/0000-0002-1381-9125
Yongzhi Cai https://orcid.org/0000-0002-7714-493X
Yi Yang https://orcid.org/0000-0002-6535-8500
WeiKang Zheng https://orcid.org/0000-0002-2636-6508
Xiangcun Meng https://orcid.org/0000-0001-5316-2298
Chengyuan Wu https://orcid.org/0000-0002-2452-551X
Liping Li https://orcid.org/0009-0003-3758-0598
Zeyi Zhao https://orcid.org/0009-0005-2963-7245
J. Craig Wheeler https://orcid.org/0000-0003-1349-6538
Jose L. Prieto https://orcid.org/0000-0003-0943-0026
Jialian Liu https://orcid.org/0009-0000-0314-6273
Shengyu Yan https://orcid.org/0009-0004-4256-1209
Fangzhou Guo https://orcid.org/0009-0001-0660-1902
C. P. Gutiérrez https://orcid.org/0000-0003-2375-2064
E. Kankare https://orcid.org/0000-0001-8257-3512
Peter Lundqvist https://orcid.org/0000-0002-3664-8082
S. Moran https://orcid.org/0000-0001-5221-0243
A. Reguitti https://orcid.org/0000-0003-4254-2724
I. Salmaso https://orcid.org/0000-0003-1450-0869
M. D. Stritzinger https://orcid.org/0000-0002-5571-1833
S. Williams https://orcid.org/0000-0001-8178-0202
J.-W. Zhao https://orcid.org/0009-0009-8633-8582
D.-D Shi https://orcid.org/0000-0002-4314-5686
Jianrong Shi https://orcid.org/0000-0002-0349-7839
Z.-H. Peng https://orcid.org/0009-0000-7773-553X
Tengfei Song https://orcid.org/0000-0002-3876-6330
Attila Bódi https://orcid.org/0000-0002-8585-4544
Borbála Cseh https://orcid.org/0000-0002-6497-8863
Ágoston Horti-Dávid https://orcid.org/0009-0008-2052-8474
Csilla Kalup https://orcid.org/0000-0002-1663-0707
Levente Kriskovics https://orcid.org/0000-0002-1792-546X
Réka Könyves-Tóth https://orcid.org/0000-0002-8770-6764
András Pál https://orcid.org/0000-0001-5449-2467
Bálint Seli https://orcid.org/0000-0002-3658-2175
Ádám Sódor https://orcid.org/0000-0001-7806-2883
Róbert Szakáts https://orcid.org/0000-0002-1698-605X
P. A. Mazzali https://orcid.org/0000-0001-6876-8284
T. Kravtsov https://orcid.org/0000-0003-0955-9102
K. Matilainen https://orcid.org/0000-0002-8111-4581
T. M. Reynolds https://orcid.org/0000-0002-1022-6463
L. Galbany https://orcid.org/0000-0002-1296-6887
Bo Wang https://orcid.org/0000-0002-3231-1167

References

Aldering, G., Antilogus, P., Bailey, S., et al. 2006, ApJ, 650, 510
Arcavi, I., Howell, D. A., Kasen, D., et al. 2017, Natur, 551, 210
Arnett, W. D. 1982, ApJ, 253, 785
Asplund, M., Grevesse, N., Sauval, A. J., & Scott, P. 2009, ARA&A, 47, 481
Bellm, E. C., Kulkarni, S. R., Graham, M. J., et al. 2019, PASP, 131, 018002
Blondin, S., Dessart, L., & Hillier, D. J. 2015, MNRAS, 448, 2766
Blondin, S., Dessart, L., & Hillier, D. J. 2018, MNRAS, 474, 3931
Bloom, J. S., Kasen, D., Shen, K. J., et al. 2012, ApJL, 744, L17
Borish, H. J., Huang, C., Chevalier, R. A., et al. 2015, ApJ, 801, 7
Bruzual, G., & Charlot, S. 2003, MNRAS, 344, 1000
Byler, N., Dalcanton, J., Conroy, C., & Johnson, B. 2017, ApJ, 840, 44
Calzetti, D., Armus, L., Bohlin, R., et al. 2000, ApJ, 533, 682
Chevalier, R. A., & Fransson, C. 1994, ApJ, 420, 268
Childress, M., Aldering, G., Aragon, C., et al. 2011, ApJ, 733, 3
Childress, M. J., Scalzo, R. A., Sim, S. A., et al. 2013, ApJ, 770, 29
Chugai, N. N. 2001, MNRAS, 326, 1448
Chugai, N. N., Chevalier, R. A., & Lundqvist, P. 2004, MNRAS, 355, 627
Chugai, N. N., & Yungelson, L. R. 2004, AstL, 30, 65
Deng, J., Kawabata, K. S., Ohyama, Y., et al. 2004, ApJL, 605, L37
Fan, Y.-F., Bai, J.-M., Zhang, J.-J., et al. 2015, RAA, 15, 918
Filippenko, A. V. 1982, PASP, 94, 715
Filippenko, A. V., Richmond, M. W., Matheson, T., et al. 1992, ApJL, 384, L15
Firth, R. E., Sullivan, M., Gal-Yam, A., et al. 2015, MNRAS, 446, 3895
Fransson, C., Ergon, M., Challis, P. J., et al. 2014, ApJ, 797, 118
Graham, M. J., Kulkarni, S. R., Bellm, E. C., et al. 2019, PASP, 131, 078001
Hachisu, I., Kato, M., & Nomoto, K. 1999, ApJ, 522, 487
Hamuy, M., Phillips, M. M., Suntzeff, N. B., et al. 2003, Natur, 424, 651
Han, Y., Fan, L., Zheng, X. Z., Bai, J.-M., & Han, Z. 2023, ApJS, 269, 39
Han, Z., & Podsiadlowski, P. 2004, MNRAS, 350, 1301

Han, Z., & Podsiadlowski, P. 2006, MNRAS, 368, 1095
Hicken, M., Challis, P., Kirshner, R. P., et al. 2012, ApJS, 200, 12
Hicken, M., Garnavich, P. M., Prieto, J. L., et al. 2007, ApJL, 669, L17
Hillebrandt, W., Sim, S. A., & Röpke, F. K. 2007, A&A, 465, L17
Howell, D. A. 2011, NatCo, 2, 350
Howell, D. A., Sullivan, M., Nugent, P. E., et al. 2006, Natur, 443, 308
Hsiao, E. Y., Conley, A., Howell, D. A., et al. 2007, ApJ, 663, 1187
Hu, L., Chen, X., & Wang, L. 2022, ApJ, 930, 70
Kasen, D. 2010, ApJ, 708, 1025
Kashi, A., & Soker, N. 2011, MNRAS, 417, 1466
Kobulnicky, H. A., & Kewley, L. J. 2004, ApJ, 617, 240
Landolt, A. U. 1992, AJ, 104, 340
Lee, H., Chonis, T. S., Hill, G. J., et al. 2010, SPIE, 7735, 77357H
Leonard, D. C. 2007, ApJ, 670, 1275
Li, L., Zhai, Q., Zhang, J., & Wang, X. 2022, TNSCR, 2022-701, 1
Liu, D., Wang, B., & Han, Z. 2018, MNRAS, 473, 5352
Maeda, K., Kawabata, K., Li, W., et al. 2009, ApJ, 690, 1745
Magnier, E. A., Schlafly, E. F., Finkbeiner, D. P., et al. 2020, ApJS, 251, 6
Maoz, D., Mannucci, F., & Nelemans, G. 2014, ARA&A, 52, 107
Matzner, C. D., & McKee, C. F. 1999, ApJ, 510, 379
Meng, X., & Podsiadlowski, P. 2018, ApJ, 861, 127
Meng, X., Yang, W., & Geng, X. 2009, PASJ, 61, 1251
Miller, J., & Stone, R. 1994, The Kast Double Spectrograph Tech. Rep. 66., Lick Observatory
Moriya, T. J., Maeda, K., Taddia, F., et al. 2013, MNRAS, 435, 1520
Munari, U., Henden, A., Belligoli, R., et al. 2013, NewA, 20, 30
Nomoto, K., Kobayashi, C., & Tominaga, N. 2013, ARA&A, 51, 457
Nugent, P. E., Sullivan, M., Cenko, S. B., et al. 2011, Natur, 480, 344
Ofek, E. O., Lin, L., Kouveliotou, C., et al. 2013, ApJ, 768, 47
Ofek, E. O., Sullivan, M., Shaviv, N. J., et al. 2014, ApJ, 789, 104
Pakmor, R., Kromer, M., Taubenberger, S., & Springel, V. 2013, ApJL, 770, L8
Parrent, J. T., Howell, D. A., Friesen, B., et al. 2012, ApJL, 752, L26
Patat, F., Chandra, P., Chevalier, R., et al. 2007, Sci, 317, 924
Perlmutter, S., Aldering, G., Goldhaber, G., et al. 1999, ApJ, 517, 565
Phillips, M. M. 1993, ApJL, 413, L105
Phillips, M. M., Ashall, C., Brown, P. J., et al. 2024, ApJS, 273, 16
Phillips, M. M., Wells, L. A., Suntzeff, N. B., et al. 1992, AJ, 103, 1632
Prieto, J. L., Garnavich, P. M., Phillips, M. M., et al. 2007, arXiv:0706.4088
Riess, A. G., Filippenko, A. V., Challis, P., et al. 1998, AJ, 116, 1009
Riess, A. G., Yuan, W., Macri, L. M., et al. 2022, ApJL, 934, L7
Sasdelli, M., Mazzali, P. A., Pian, E., et al. 2014, MNRAS, 445, 711
Scalzo, R. A., Aldering, G., Antilogus, P., et al. 2010, ApJ, 713, 1073
Schlafly, E. F., & Finkbeiner, D. P. 2011, ApJ, 737, 103
Schmidt, B. P., Kirshner, R. P., Leibundgut, B., et al. 1994, ApJL, 434, L19
Sharma, Y., Sollerman, J., Fremling, C., et al. 2023, ApJ, 948, 52
Silverman, J. M., Foley, R. J., Filippenko, A. V., et al. 2012, MNRAS, 425, 1789
Silverman, J. M., Ganeshalingam, M., Li, W., et al. 2011, MNRAS, 410, 585
Silverman, J. M., Nugent, P. E., Gal-Yam, A., et al. 2013, ApJS, 207, 3
Skrutskie, M. F., Cutri, R. M., Stiening, R., et al. 2006, AJ, 131, 1163
Smith, K. W., Smartt, S. J., Young, D. R., et al. 2020, PASP, 132, 085002
Smith, N. 2017, in Handbook of Supernovae, ed. A. W. Alsabti & P. Murdin (Springer), 403
Smith, N., Silverman, J. M., Filippenko, A. V., et al. 2012, AJ, 143, 17
Soker, N. 2011, arXiv:1109.4652
Stahl, B. E., Zheng, W., de Jaeger, T., et al. 2019, MNRAS, 490, 3882
Sternberg, A., Gal-Yam, A., Simon, J. D., et al. 2011, Sci, 333, 856
Stoll, R., Prieto, J. L., Stanek, K. Z., et al. 2011, ApJ, 730, 34
Stritzinger, M., & Leibundgut, B. 2005, A&A, 431, 423
Stritzinger, M., Taddia, F., Fransson, C., et al. 2012, ApJ, 756, 173
Tanaka, M., Kawabata, K. S., Yamanaka, M., et al. 2010, ApJ, 714, 1209
Taubenberger, S., Benetti, S., Childress, M., et al. 2011, MNRAS, 412, 2735
Tonry, J., Denneau, L., Weiland, H., et al. 2022, TNSTR, 2022-679, 1
Tonry, J. L., Denneau, L., Heinze, A. N., et al. 2018, PASP, 130, 064505
Uno, K., Maeda, K., Nagao, T., et al. 2023a, ApJ, 944, 203
Uno, K., Nagao, T., Maeda, K., et al. 2023b, ApJ, 944, 204
van Zee, L., & Haynes, M. P. 2006, ApJ, 636, 214
Wang, B. 2018, RAA, 18, 049
Wang, B., Justham, S., Liu, Z.-W., et al. 2014, MNRAS, 445, 2340
Wang, B., Zhou, W.-H., Zuo, Z.-Y., et al. 2017, MNRAS, 464, 3965
Wang, C.-J., Bai, J.-M., Fan, Y.-F., et al. 2019, RAA, 19, 149
Wang, L., Baade, D., Höflich, P., et al. 2004, ApJL, 604, L53
Wang, L., Hu, M., Wang, L., et al. 2024, NatAs, 8, 504
Wang, X., Li, W., Filippenko, A. V., et al. 2009, ApJ, 697, 380
Wood-Vasey, W. M., Wang, L., & Aldering, G. 2004, ApJ, 616, 339
Yamanaka, M., Kawabata, K. S., Kinugasa, K., et al. 2009, ApJL, 707, L118
Yang, Y., Baade, D., Hoeflich, P., et al. 2023, MNRAS, 519, 1618
Yaron, O., & Gal-Yam, A. 2012, PASP, 124, 668
Yuan, F., Quimby, R. M., Wheeler, J. C., et al. 2010, ApJ, 715, 1338
Zhai, Q., Zhang, J.-J., Lin, W., et al. 2025, ApJ, 978, 163
Zhang, J.-C., Fan, Z., Yan, J.-Z., et al. 2016, PASP, 128, 105004
Zhang, J.-J., Wang, X., József, V., et al. 2020, MNRAS, 498, 84
Zhang, J.-J., Wang, X.-F., Sasdelli, M., et al. 2016, ApJ, 817, 114
Zhang, K., Wang, X., Zhang, J.-J., et al. 2016, ApJ, 820, 67
Zhang, T., Wang, X., Wu, C., et al. 2012, AJ, 144, 131